Novel function for AP-1B during cell migration

Margaret Johnson Kell†, Su Fen Ang†, Lucy Pigati, Abby Halpern, and Heike Fölsch*
Department of Cell and Developmental Biology, Northwestern University Feinberg School of Medicine, Chicago, IL 60611

ABSTRACT **The epithelial cell-specific clathrin adaptor protein (AP)-1B has a well-established role in polarized sorting of cargos to the basolateral membrane. Here we show that β1 integrin was dependent on AP-1B and its coadaptor, autosomal recessive hypercholesterolemia protein (ARH), for sorting to the basolateral membrane. We further demonstrate an unprecedented role for AP-1B at the basal plasma membrane during collective cell migration of epithelial sheets. During wound healing, expression of AP-1B (and ARH in AP–1B-positive cells) slowed epithelial-cell migration. We show that AP-1B colocalized with β1 integrin in focal adhesions during cell migration using confocal microscopy and total internal reflection fluorescence microscopy on fixed specimens. Further, AP-1B labeling in cell protrusions was distinct from labeling for the endocytic adaptor complex AP-2. Using stochastic optical reconstruction microscopy we identified numerous AP–1B-coated structures at or close to the basal plasma membrane in cell protrusions. In addition, immunoelectron microscopy showed AP-1B in coated pits and vesicles at the plasma membrane during cell migration. Lastly, quantitative real-time reverse transcription PCR analysis of human epithelial-derived cell lines revealed a loss of AP-1B expression in highly migratory metastatic cancer cells suggesting that AP-1B's novel role at the basal plasma membrane during cell migration might be an anticancer mechanism.**

Monitoring Editor
Avital Rodal
Brandeis University

Received: Apr 22, 2020
Revised: Aug 10, 2020
Accepted: Aug 11, 2020

INTRODUCTION

Organ cavities are lined with columnar epithelial cells that organize apical domains luminally, whereas basolateral domains are contacting neighboring cells and the basement membrane. This organized monolayer architecture has to be maintained throughout life to avoid diseases such as metastatic cancer and polycystic kidney disease (Mellman and Nelson, 2008). To ensure this, polarized epithelial cells continuously sort membrane receptors and adhesion molecules to either surface domain (Rodriguez-Boulan *et al.*, 2004; Weisz and Rodriguez-Boulan, 2009; Weisz and Fölsch, 2016). However, little is known about the involvement or behavior of the polarized sorting machinery during epithelial wound healing.

Major sorting stations for the polarized delivery of cargos to the plasma membrane are the *trans*-Golgi network (TGN) during biosynthesis and recycling endosomes (REs) for sorting of endocytic cargos and biosynthetic cargos that reach REs from the TGN (Ang *et al.*, 2004; Cancino *et al.*, 2007; Gravotta *et al.*, 2007; Fölsch *et al.*, 2009; Ang and Fölsch, 2012). Basolateral sorting in REs depends on adaptor protein (AP)-1B (Gravotta *et al.*, 2007; Fölsch, 2015b). AP-1B is a heterotetrameric clathrin adaptor that shares its two large γ and β1 and its small σ1 subunit with AP-1A (Fölsch *et al.*, 1999). The only difference between both complexes is the incorporation of their respective medium subunits μ1B or μ1A. Unlike μ1A, μ1B is tissue specific and its expression was found restricted to columnar epithelial cells with the exception of the kidney cell line Lilly laboratories cell porcine kidney (LLC-PK1) that polarizes but does not express μ1B (Roush *et al.*, 1998; Ohno *et al.*, 1999). LLC-PK1 cells are

This article was published online ahead of print in MBoC in Press (http://www.molbiolcell.org/cgi/doi/10.1091/mbc.E20-04-0256) on August 20, 2020.
The authors declare no competing financial interests.

†These authors contributed equally.

Author contributions: Conceptualization: S.F.A., M.J.K., and H.F.; formal analysis: S.F.A., M.J.K., L.P., and H.F.; investigation: S.F.A., M.J.K., L.P., A.H., and H.F.; writing original draft: H.F.; editing and review: S.F.A., M.J.K., L.P., A.H., and H.F.; visualization: S.F.A., M.J.K., and H.F.; supervision: H.F.; funding acquisition: S.F.A., and H.F.

*Address correspondence to: Heike Fölsch (h-folsch@northwestern.edu).

Abbreviations used: AP, adaptor protein; ARH, autosomal recessive hypercholesterolemia protein; BSA, bovine serum albumin; CHC, clathrin heavy chain; EM, electron microscopy; FBS, fetal bovine serum; GAPDH, glyceraldehyde 3-phosphate dehydrogenase; GGA, Golgi-localized gamma-ear containing protein; HBE, human bronchial epithelial; immuno-EM, immunoelectron microscopy; LLC-PK1, Lilly laboratories cell porcine kidney; MDCK, Madin-Darby canine kidney; PBS, phosphate-buffered saline; $PI(3,4,5)P_3$, phosphatidylinositol 3,4,5-trisphosphate; qRT-PCR, quantitative real-time reverse transcription PCR; RE, recycling endosome; RT, room temperature; shRNA, short hairpin RNA; STORM, stochastic optical reconstruction microscopy; TGN, *trans*-Golgi network; TIRF, total internal reflection fluorescence; YFP, yellow fluorescent protein.

understood to be derived from renal proximal tubules that are naturally devoid of AP-1B expression (Roush *et al.*, 1998; Schreiner *et al.*, 2010). Since its discovery, LLC-PK1 cell lines with or without exogenous expression of μ1B to restore AP-1B function have been widely used to analyze polarized protein sorting (Fölsch, 2015a). Like other members of the family of heterotetrameric adaptor complexes such as AP-1A, AP-2, AP-3, and AP-4, AP-1B directly recognizes cargos with YxxØ tyrosine-based motifs via μ1B and (D/E)xxxL(L/I) dileucine motifs, LL-motifs for short, through a shared surface between σ1 and γ adaptin (Ohno *et al.*, 1999; Janvier *et al.*, 2003; Doray *et al.*, 2007).

Noticeably, although highly homologous, we and others found that AP-1A and AP-1B are functionally distinct. Whereas AP-1A is largely localized at the TGN and in early endosomes, AP-1B localizes and functions in REs of fully polarized epithelial cells (Fölsch *et al.*, 2001; Gan *et al.*, 2002; Gravotta *et al.*, 2007). Although their localization as judged by immunofluorescence may appear mixed (Guo *et al.*, 2013), the careful biochemical analysis showed that both complexes do not form mixed vesicle populations (Fölsch *et al.*, 2003). Moreover, both AP-1A and AP-1B facilitated basolateral sorting from the TGN and REs, respectively, and thus have overlapping roles in the sorting of some, but not all, surface receptors (Fölsch *et al.*, 1999; Kang and Fölsch, 2011; Gravotta *et al.*, 2012; Caceres *et al.*, 2019).

AP-1B selectively worked together with the coadaptor autosomal recessive hypercholesterolemia protein (ARH) for sorting of an artificial cargo with FxNPxY signal (Kang and Fölsch, 2011). However, it remained to be shown if AP-1B and ARH would also cooperate in the sorting of endogenous cargos such as the focal adhesion molecule β1 integrin that contains FxNPxY sorting motifs (Moser *et al.*, 2009). The interaction between ARH and AP-1B was mediated via the large β1 adaptin subunit (He *et al.*, 2002; Mishra *et al.*, 2002; Kang and Fölsch, 2011), and both AP-1A and AP-1B were pulled down by ARH in vitro; however, AP-1A did not cooperate with ARH in cells (see Figure 1A for a summary of known binding partners for AP-1B [Kang and Fölsch, 2011]). Most likely, the lipid environment present at the TGN that is enriched with phosphatidylinositol 4-phosphate (PI(4)P; Wang *et al.*, 2003) may not be amicable for ARH recruitment in contrast to REs (Mishra *et al.*, 2002). Indeed, AP-1B expression in epithelial cells led to an accumulation of phosphatidylinositol 3,4,5-trisphosphate ($PI(3,4,5)P_3$) in REs, and in turn we also found that AP-1B localization in REs depended on $PI(3,4,5)P_3$ (Fields *et al.*, 2010). This recruitment was mediated by μ1B, because mutations in a specific region of its cytosolic domain (R338N/N339S/V340E) that aligns with the $PI(4,5)P_2$ binding patch of μ2 (Collins *et al.*, 2002) led to a loss of RE localization (Fields *et al.*, 2010). In addition to $PI(3,4,5)P_3$, we identified Arf6 as important for AP-1B function (Shteyn *et al.*, 2011). Arf6 precipitated AP-1A and AP-1B in in vitro pull downs, and mutant Arf6 disrupted AP-1B sorting function in polarized cells (compare Figure 1A; Shteyn *et al.*, 2011). Exogenous overexpression of Arf6 in LLC-PK1 cells grown in cell clusters induced ruffling. Importantly, only AP-1B but not AP-1A was recruited into these membrane ruffles (Shteyn *et al.*, 2011). However, the role that AP-1B might play in membrane ruffles remained elusive.

It is generally accepted that whereas AP-2 facilitates clathrin-mediated endocytosis, all other heterotetrameric AP complexes facilitate sorting at the TGN or in endosomes (Hirst and Robinson, 1998; Boehm and Bonifacino, 2001; Nakatsu and Ohno, 2003). However, studies on ubiquitously expressed adaptor complexes are typically not performed in epithelial cells. Moreover, studies on AP-1B are typically performed in polarized cells grown in monolayers or cell clusters that are devoid of membrane ruffles. In this study, we demonstrate that in addition to its role in REs, AP-1B localizes to the plasma membrane in cell protrusions. This was not seen before, because LLC-PK1 cells typically don't form membrane ruffles when grown in clusters or as monolayers for multiple days before immunofluorescence staining. However, LLC-PK1 cells start to ruffle and migrate when induced through Arf6 expression (Shteyn *et al.*, 2011) or wounding of monolayers as presented in this study. Importantly, AP-1B localized in areas at the plasma membrane that were distinct from AP–2-positive areas. We further found that β1 integrin was an AP-1B and ARH cargo protein, and β1 integrin colocalized with AP-1B in cell protrusions during cell migration. Moreover, expression of AP-1B and ARH in AP–1B-positive cells slowed the speed of collective cell migration. Only AP-1B but not ARH expression was lost in highly metastatic cancer cells suggesting that AP-1B's function during collective cell migration might be physiologically relevant.

RESULTS

Creation of LLC-PK1 cells stably expressing AP-1B-YFP

Because we found that AP-1B was recruited into cell protrusions facilitated by Arf6 (Shteyn *et al.*, 2011), we wondered if AP-1B might localize to focal adhesions and play a role in cell migration. Focal adhesions are formed by integrin heterodimers, consisting of an α and a β integrin chain, that are attached to the extracellular matrix (Horton *et al.*, 2016). They are necessary for forward movement, and integrin heterodimers that contain β1 integrin are well known for their role in generating speed during cell migration (Paul *et al.*, 2015; Horton *et al.*, 2016). Thus, to analyze a potential role for AP-1B in cell migration, we sought to test if 1) β1 integrin might be recognized as a cargo protein of AP-1B (and ARH), 2) if AP-1B expression might influence cell migration speed, and 3) if AP-1B might colocalize with β1 integrin during collective cell migration. To facilitate our studies, we created stable LLC-PK1 cell lines that expressed μ1A or μ1B with internal yellow fluorescent protein (YFP) tags as there are no suitable antibodies that would distinguish between μ1A/AP-1A and μ1B/AP-1B by immunofluorescence. The YFP-tags were placed between amino acids 230 and 231 as previously described for HA-tagged variants and guided by the crystal structure of μ2 (Owen and Evans, 1998; Fölsch *et al.*, 2001). The newly created cell lines had modest expression levels as compared with endogenous μ1A, and comparable to the expression levels of the HA-tagged variants in LLC-PK1::μ1A-HA and LLC-PK1::μ1B-HA cell lines that were established earlier (Supplemental Figure S1A; Fölsch *et al.*, 2001). Importantly, anti-GFP immunoprecipitations of μ1A-YFP and μ1B-YFP coprecipitated γ-adaptin indicating that they were incorporated into AP-1A-YFP and AP-1B-YFP complexes, respectively (Supplemental Figure S1B).

To test if AP-1B-YFP was incorporated into clathrin-coated vesicles, we seeded LLC-PK1::μ1B-YFP cells in 20-cm dishes. Monolayers were wounded with multiple scratches to create several wound edges throughout the surface of the plates and allowed to migrate for several hours before cells were homogenized and crude clathrin-coated vesicles were harvested by centrifugation in 1% Triton X-100 (Pearse, 1982) to mimic wound healing assays used in this study. Pellets were resuspended in a sucrose buffer and subjected to immunoisolations (Fölsch *et al.*, 2003) with anti-GFP or anti-γ-adaptin antibodies followed by SDS–PAGE and Western blot (Figure S1, C and D). AP-1B-YFP was brought down in both immunoprecipitations. As expected, anti-GFP antibodies coprecipitated γ-adaptin and clathrin heavy chain (CHC), but not μ1A, consistent with our previous findings that AP-1A and AP-1B form biochemically distinct vesicle populations (Fölsch *et al.*, 2003). Furthermore, anti-γ-adaptin

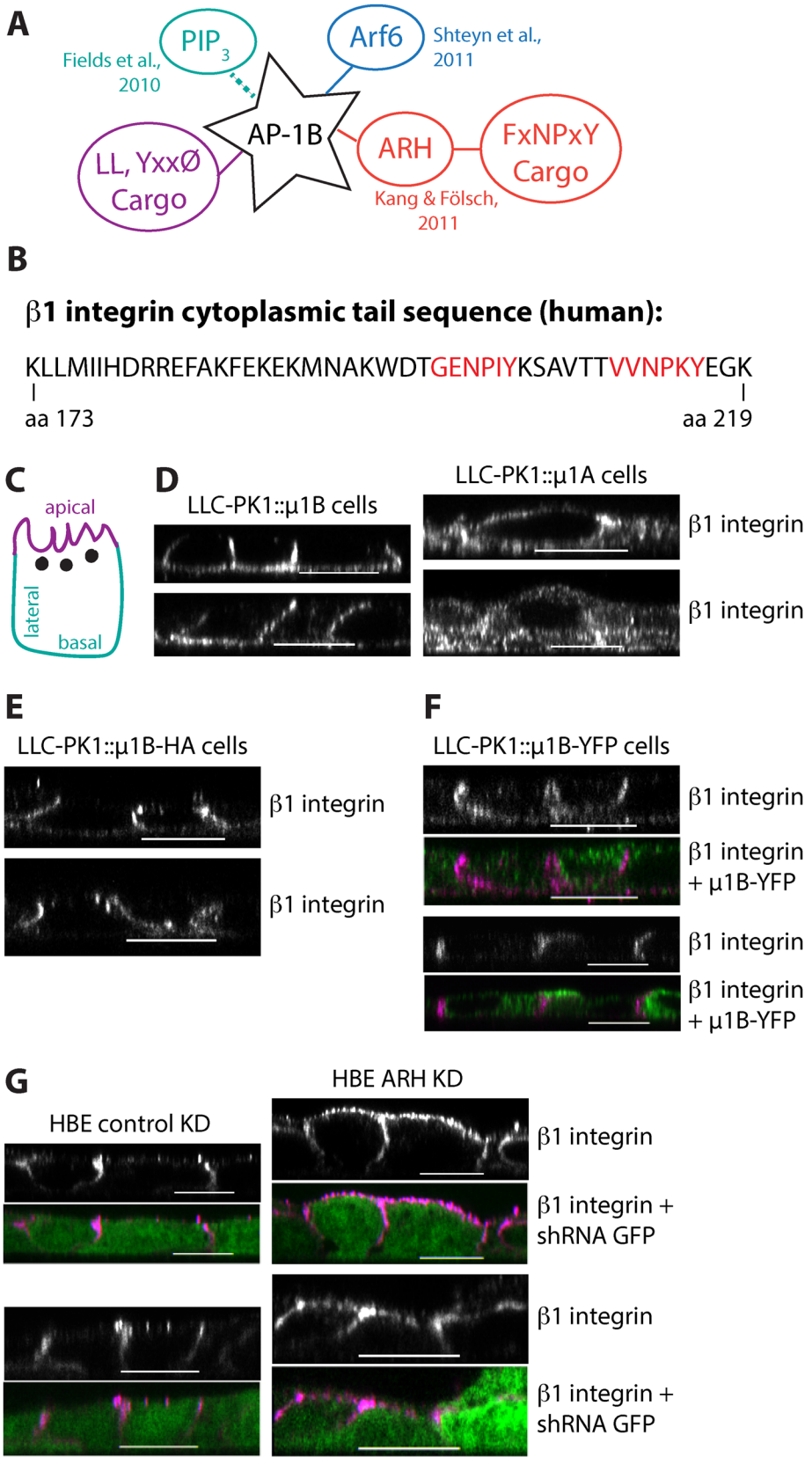

FIGURE 1: AP-1B and ARH are necessary for β1 integrin sorting. (A) Schematic depiction of known protein partners of AP-1B. Solid lines indicate direct interactions based on coimmunoprecipitations, yeast 2-hybrid assays, and/or cell culture experiments. Punctate line between AP-1B and PI(3,4,5)P_3 (= PIP_3) indicates suspected interaction based on cell culture experiments. (B) Schematic depiction of the cytoplasmic tail of human β1 integrin. FxNPxY motifs are annotated in red. (C) Schematic depicting apical, basal, and lateral membrane organization of polarized cells; black dots represent endosomes. (D–F) LLC-PK1::μ1B cells (D, left panels) and LLC-PK1::μ1A cells (D, right panels), LLC-PK1::μ1B-HA cells (E), and LLC-PK1::μ1B-YFP cells (F, cells with green signals express μ1B-YFP) were gown on filter supports for 4 d with gentle rocking from side-to-side for 3 d prior to fixation. After fixation, cells were stained for β1 integrin (magenta in F). (G) HBE cells depleted of GAPDH (left panels) or ARH (right panels) were grown on Matrigel-coated filter supports for 4 d. Subsequently, cells were fixed and stained for β1 integrin (magenta). GFP expression indicates shRNA presence. (D–G) Specimens were analyzed by confocal microscopy and representative cross-sections through assembled 3D galleries are shown. Bars are 10 μm.

antibodies coprecipitated μ1B-YFP and endogenous μ1A as well as CHC. We conclude that AP-1B-YFP was incorporated into clathrin-coated vesicles that were distinct from AP-1A vesicles.

β1 integrin is an AP-1B (and ARH) cargo protein

β1 integrin has two FxNPxY motifs in its cytoplasmic tail (GENPIY and VVNPKY, Figure 1B; Moser *et al.*, 2009) that have been reported to interact with endocytic coadaptors such as Dab2, numb, and ARH (Traub, 2009). Previously, we showed that ARH cooperated with AP-1B in REs to facilitate basolateral sorting of a model cargo protein with an FxNPxY motif (Kang and Fölsch, 2011). Therefore, we asked if β1 integrin depended on AP-1B (and ARH) for basolateral sorting in epithelia. To this end, we tested polarized sorting of β1 integrin in LLC-PK1 cells stably expressing μ1A (LLC-PK1::μ1A) or μ1B (LLC-PK1::μ1B) seeded on filter supports to allow for polarization. A basolateral-localized transmembrane protein is deemed an AP-1B cargo if it is sorted correctly to the basolateral membrane in the presence of AP-1B, but missorted in its absence (Fölsch *et al.*, 1999; Fölsch, 2015a). Polarized cells were fixed and stained with antibodies directed against β1 integrin. Indeed, whereas β1 integrin was correctly sorted to the basolateral membrane in LLC-PK1::μ1B cells, β1 integrin was in part missorted to the apical membrane as well as endosomal puncta in LLC-PK1::μ1A cells (Figure 1D, compare schematic in Figure 1C). Note the disorganized appearance of LLC-PK1::μ1A cells that was also a feature of parental LLC-PK1 cells in the absence of AP-1B (Roush *et al.*, 1998;

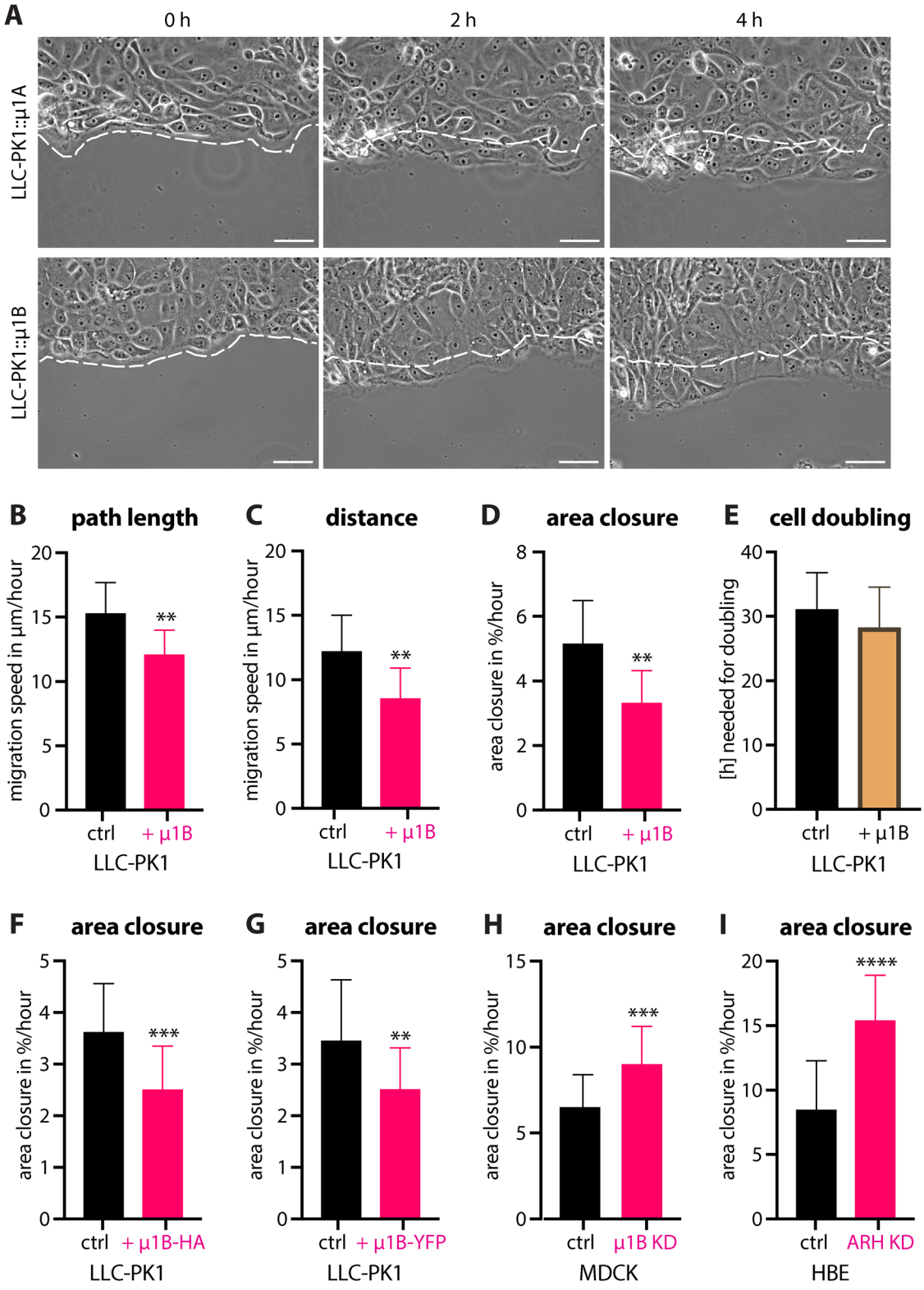

FIGURE 2: AP-1B expression in epithelial cells slows down migration speeds. LLC-PK1, MDCK, and HBE cells were grown in Matrigel-coated MatTek dishes typically for 2 d. After wounding, cells were transferred to a Nikon BioStation for live imaging for up to 4 h. (A) Selected still images of LLC-PK1::µ1A (top panels) and LLC-PK1::µ1B (bottom panels) wounded monolayers at the beginning (0 h), 2 h, and 4 h after the start of data acquisition. Images of selected areas at the wound edge were taken every 15 min. Pixeled lines indicate wound edges at the beginning of live imaging. Bars are 50 µm. (B and C) Traveled path length (B) and distance (C) of migrating LLC-PK1 cells were determined using manual tracking of individual cells at the wound edge as described in *Materials and Methods*. Data represent mean values from three independent experiments. LLC-PK1::µ1A: cells from nine different areas (a total of 55 individual cells) were analyzed; LLC-PK1::µ1B: cells from 14 different areas (a total of 70 individual cells) were analyzed. (D) Area closure data

Fölsch *et al.*, 1999). Moreover, β1 integrin was also correctly sorted to the basolateral membrane in LLC-PK1::μ1B-HA and LLC-PK1::μ1B-YFP cells (Figure 1, E and F) indicating that the internal tags did not interfere with the sorting function of AP-1B. In addition, β1 integrin was missorted in Madin-Darby canine kidney (MDCK) cells depleted of μ1B (Gravotta *et al.*, 2007). Therefore, basolateral sorting of β1 integrin depends on AP-1B.

To test if ARH cooperated with AP-1B in β1 integrin sorting, we depleted ARH or glyceraldehyde 3-phosphate dehydrogenase (GAPDH) as control in human bronchial epithelial (HBE) cells with short hairpin RNA (shRNA) vectors that also express GFP to indicate cells that are positive for shRNA expression using previously established protocols (Kang and Fölsch, 2011). In control HBE cells depleted of GAPDH, β1 integrin was correctly sorted to the basolateral membrane in addition to a few endosomal puncta. In contrast, β1 integrin was nonpolarized and partially missorted to the apical membrane after ARH depletion (Figure 1G). Note that we previously showed that depletion of ARH specifically affected basolateral sorting of FxNPxY-cargo proteins, but did not interfere with the basolateral sorting of cargos with YxxØ and LL-signals (Kang and Fölsch, 2011). We conclude that basolateral sorting of β1 integrin depends on both AP-1B and ARH. Thus, in addition to the previously identified artificial cargo protein LDLR-CT27, we here identify β1 integrin as an endogenous cargo for AP-1B and its coadaptor ARH.

In summary, we generated cell lines stably expressing tagged forms of μ1B that are fully functional and we established the focal adhesion marker β1 integrin as an AP-1B (and ARH) cargo protein.

AP-1B expression slows down cell migration

β1 integrin is important for the generation of speed during cell migration (Paul *et al.*, 2015). Because we found that β1 integrin is an AP–1B-dependent cargo protein, we wondered if AP-1B expression might influence the speed of collective cell migration. Thus, we seeded LLC-PK1::μ1A or LLC-PK1::μ1B cells on MatTek dishes coated with 1 mg/ml Matrigel. Cell monolayers were wounded and migration during wound healing was observed live in a Nikon BioStation for up to 4 h. Images of selected areas of the wound edge were taken every 15 min (Supplemental Videos figure2_AP1A.mov and figure2_AP1B.mov). Note the lack of dividing cells. Figure 2A shows still images at the beginning, after 2 h, and after 4 h of imaging. Using Nikon Elements software, individual cells at the wound edge were tracked manually to determine their traveled path length and distance (Figure 2, B and C). LLC-PK1::μ1A cells migrated with an average speed of 15.3 μm/h as opposed to 12.1 μm/h for LLC-PK1::μ1B cells, a reduction of 21%. This difference was statistically significant ($P < 0.002$) and was not a result of lost directionality. When migration speeds were determined assessing the "straight" distance, LLC-PK1::μ1A cells traveled at a rate of 12.2 μm/h, whereas LLC-PK1::μ1B cells traveled 8.5 μm/h, a 31% reduction in migration speed ($P < 0.003$). Finally, we determined migration prowess by analyzing the total covered area of the migrating cells (Figure 2D). Whereas LLC-PK1::μ1A cells covered 5.2% of the total area of the imaged field per hour, LLC-PK1::μ1B cells covered only 3.3% of the total area per hour, a 37% reduction ($P < 0.002$). Although we rarely observed dividing cells during wound healing assays, growth rates were determined by counting cells at 0 and 48 h after seeding on coverglass coated with 1 mg/ml Matrigel. As expected, the times needed for cell numbers to double were comparable between LLC-PK1::μ1A cells (31 h) and LLC-PK1::μ1B cells (28 h) and therefore were not responsible for the observed differences in migration speeds (Figure 2E). Furthermore, we detected no differences in the arrangement of actin, microtubule, or keratin cytoskeleton at the leading edge between LLC-PK1::μ1A and LLC-PK1::μ1B cells (unpublished data, and compare actin staining in Figures 3 and 4).

In conclusion, using three different means of analyzing migration speeds, we found that the presence of AP-1B in LLC-PK1 cells slowed down cell migration in wound healing assays.

Importantly, the cell lines expressing HA or YFP-tagged μ1B/AP-1B also migrated at a slower pace as compared with the cell lines expressing the correspondingly tagged μ1A/AP-1A. Whereas LLC-PK1::μ1A-HA cells covered 3.6% of the total area per hour, LLC-PK1::μ1B-HA cells covered only 2.5% of the total area per hour, a 31% reduction (Figure 2F, $P < 0.0003$). Moreover, LLC-PK1::μ1A-YFP cells covered 3.5% of the observed area per hour compared with 2.5% coverage achieved by LLC-PK1::μ1B-YFP cells, a 29% reduction (Figure 2G, $P < 0.006$).

To make sure that the effect of AP-1B on cell migration was not specific to LLC-PK1 cells, we depleted μ1B expression in MDCK cells with shRNA using previously established protocols (Anderson *et al.*, 2005; Fields *et al.*, 2010) and determined migration speeds through area closure analysis (Figure 2H). Whereas mock-depleted MDCK cells covered 6.5% of the total area per hour, μ1B-depleted MDCK cells were able to cover 9% of the total area per hour, an increase by 38% ($P < 0.0002$). Thus, using gain-of-function and loss-of-function approaches, we found that AP-1B presence in epithelial cells decreased their migration speeds.

Previously, depleting ARH in cells without AP-1B expression led to a decrease in migration speed (Ezratty *et al.*, 2009). Because we found that β1 integrin depended on both AP-1B and ARH for basolateral sorting (Figure 1), we next asked how ARH depletion would affect collective cell migration in AP–1B-positive cells. Therefore, we seeded HBE cells depleted of ARH or GAPDH as control on MatTek dishes coated with 1 mg/ml Matrigel and determined migration speeds in wound healing assays. Area closure analysis showed that

represent mean values from three independent experiments. LLC-PK1::μ1A: seven independent areas were analyzed; LLC-PK1::μ1B: 15 independent areas were analyzed. (E) 8×10^5 LLC-PK1::μ1A and LLC-PK1::μ1B were seeded on coverglass coated with 1 mg/ml Matrigel. After 48 h cells were trypsinized and counted to determine the time needed for cell doubling (two independent experiments). (F and G) Area closure analysis was performed on migrating LLC-PK1 cells stably expressing μ1A-HA or μ1B-HA (F) and μ1A-YFP or μ1B-YFP (G). Data represent mean values from at least three independent experiments. LLC-PK1::μ1A-HA: 15 independent areas; LLC-PK1::μ1B-HA: 32 independent areas; LLC-PK1::μ1A-YFP: 16 independent areas; and LLC-PK1::μ1B-YFP: 22 independent areas were analyzed. (H) Area closure analysis of mock or μ1B-depleted MDCK cells. Data represent mean values from at least three independent experiments using cells from three independent KDs. Control MDCK cells: 23 independent areas; μ1B-depleted MDCK cells: 25 independent areas were analyzed. (I) Migrating HBE cells depleted of ARH or GAPDH as control were analyzed for area closure during wound healing. Area closure data represent mean values of at least three independent experiments using cells from three individual KDs. GAPDH KD HBE cells: 40 independent areas; ARH KD HBE cells: 32 independent areas were analyzed. (H and I) Efficiency of KD was controlled for and specificity of KD was confirmed with RT-PCR (unpublished data). (B–I) Error bars indicate SD. ****$P < 0.0001$; ***$P < 0.0003$; **$P < 0.006$. KD, knockdown.

whereas control HBE cells only covered 8.5% of the total area per hour, HBE cells depleted of ARH covered almost twice as much area with a speed of 15.4% of the total area per hour, an increase by 81% (Figure 2I, $P < 0.0001$). This increase in migration speed mimics the increase we saw after μ1B depletion in MDCK cells, but is in contrast to results obtained with AP–1B-negative cells (Ezratty *et al.*, 2009) and may reflect ARH functions related to AP-1B.

In summary, both the expression of AP-1B and of ARH in AP–1B-positive epithelial cells slowed down the speed of migration in wound healing assays suggesting that AP-1B may regulate processes required for cell migration.

AP-1B and β1 integrin colocalize in cell protrusions

To investigate the localization of AP-1B during cell migration and test if AP-1B colocalized with β1 integrin, we wounded monolayers of LLC-PK1::μ1B-YFP cells grown on coverglass coated with 1 mg/ml Matrigel. Subsequently, cells were allowed to migrate as sheets for up to 6 h before fixation and costaining for β1 integrin as well as the actin cytoskeleton and cell nuclei. Remarkably, confocal analysis revealed colocalization of AP-1B and β1 integrin at the edge of cell protrusions in front of actin arches (Figure 3A). To demonstrate this localization, we imaged 3D galleries throughout the specimens. Subsequently, the individual X-Y slices of the gallery were collapsed into one merged plane in a so-called "focused gallery projection" (see illustration in Figure 3A). Localization of AP-1B to β1 integrin foci was most evident in the coinciding appearance of peak intensities revealed through the line scan shown in Figure 3A. AP-1B-YFP and β1 integrin copeaked at the cell edge in ~93% of analyzed cell protrusions. Note the absence of actin staining resulting in only baseline fluorescence in the area at the plasma membrane that was enriched in AP-1B and β1 integrin.

Next we sought to further investigate AP-1B localization in cell protrusions at higher resolution. To this end, we performed total internal reflection fluorescence (TIRF) microscopy on fixed and stained specimens. TIRF microscopy detects signals that are at or in close proximity to the basal plasma membrane in an evanescent field at the coverglass–specimen interface that is typically less than 100 nm (see illustration in Figure 3B; Mattheyses *et al.*, 2010). LLC-PK1::μ1B-YFP cells were seeded on 1 mg/ml Matrigel-coated MatTek dishes. Monolayers were wounded and cells were allowed to migrate for several hours prior to fixation and costaining for β1 integrin, CHC, and the actin cytoskeleton. Subsequently, specimens were maintained in buffer and imaged the same day as soon as possible. Wound edges were scanned and well-formed protrusions were imaged. In agreement with our confocal analysis, AP-1B-YFP staining was found at the very edge of cell protrusions colocalizing with β1 integrin as indicated by arrowheads in selected insets (Figure 3B).

In contrast to AP-1B-YFP labeling, we did not observe significant colocalization of AP-1A-YFP with β1 integrin in cell protrusions of migrating LLC-PK1::μ1A-YFP cells. Indeed, when analyzed with 3D confocal microscopy, we hardly detected any AP-1A-YFP label in cell protrusions (Figure 4A). This was most evident in the baseline fluorescent intensity for AP-1A in the line scan projection. In addition, there was again a complete absence of actin staining in this area. AP-1A-YFP copeaked with β1 integrin at the cell edges in only ~33% of analyzed cell protrusions ($P = 0.0013$, Supplemental Figure S2A). Next we determined peak intensities for YFP and β1 integrin signals at the cell edges through radial line scans for cells fixed and stained either 1.5 or 6 h after wounding. Whereas the β1 integrin peak intensities were comparable for AP-1A-YFP and AP-1B-YFP cells at both time points (Supplemental Figure S2B), there was a significant increase in YFP peak intensity in AP-1B-YFP cells after 1.5 h as well as after 6 h of migration (Supplemental Figure S2C). In agreement with the confocal analysis, high-resolution TIRF revealed that AP-1A-YFP staining did not extend to the cell edges that are positive for β1 integrin and marked by arrowheads in selected insets of Figure 4B.

Next we sought to quantify colocalization of selected markers in our TIRF images. Note that although we initially imaged bigger cell areas to orient the reader, only the edges of cell protrusions were in perfect TIRF alignment due to the uneven surface of coated coverglass used in this study. Therefore, all subsequent colocalization analyses were focused on the edges of cell protrusions. Moreover, traditional colocalization analysis depends on signal intensities (Dunn *et al.*, 2011). This provides a problem with TIRF because the depth of the evanescent field is slightly different for lasers with different wavelengths, and in addition, the evanescent field decays exponentially meaning that objects further than 100 nm from the surface of the coverslip may still be excited and imaged although the signal will be less intense (Mattheyses *et al.*, 2010). Therefore, we employed an objective-based colocalization analysis that identified β1 integrin- and CHC-positive objects in AP–1–YFP-positive areas in well-formed cell protrusions as illustrated in Figure 4C (see *Materials and Methods* for further details). Data are expressed as objects in 100 YFP-positive areas to allow for comparison. Using this method, we detected 62.8 β1 integrin-positive objects within 100 AP–1B–YFP-positive areas, but only 26.2 β1 integrin-positive objects within 100 AP–1A–YFP-positive areas (Figure 4D, $P < 0.003$). In contrast and as expected, AP-1A-YFP and AP-1B-YFP showed about equal colocalization with CHC with 34 CHC-positive objects within 100 AP–1A–YFP-positive areas and 50.6 CHC-positive objects in 100 AP–1B–YFP-positive areas (Figure 4E). Lastly, 20.4% of AP–1B–YFP-positive areas contained both β1 integrin and CHC-positive objects in contrast to only 7.5% of AP–1A–YFP-positive areas containing both markers (Figure 4F, $P < 0.02$). Note the overlapping staining of both AP-1A and AP-1B with CHC is most likely underestimated, because a fully formed clathrin coat is expected to interfere with the ability of anti-GFP antibodies to label the YFP-tagged μ chains.

To summarize, AP-1B-YFP partially colocalized with β1 integrin in cell protrusions during collective cell migration. This colocalization was not observed for AP-1A-YFP.

AP-1B does not colocalize with AP-2

AP-2 is well known for its role in facilitating clathrin-mediated endocytosis of integrins (De Franceschi *et al.*, 2016; Moreno-Layseca *et al.*, 2019). Thus we wondered if AP-1B would colocalize with AP-2. To test this, we stained migrating LLC-PK1::μ1B-YFP cells with antibodies against α-adaptin, one of the large subunits of AP-2, as well as the actin cytoskeleton and analyzed the specimens with TIRF microscopy (Figure 5A). We found virtually no overlap between AP-1B-YFP and AP-2 staining. This is most obvious in the two-channel overlay of the insets. In contrast and as expected, μ1B-YFP showed colocalization with AP-1's large γ-adaptin subunit to some degree (arrowheads in selected insets, Supplemental Figure S2D). Object-based colocalization analysis revealed 29.9 α–adaptin-positive and 68.4 γ–adaptin-positive objects within 100 μ1B–YFP-positive areas (Figure 5C, $P < 0.0001$). Note that colocalization between μ1B-YFP and γ-adaptin is most likely underestimated, because γ-adaptin staining labeled both AP-1B-YFP and endogenous AP-1A. In addition, whereas μ1B-YFP labels all AP-1B-YFP complexes, anti-γ-adaptin staining probably does not stain all complexes because CHC assembly most likely interferes sterically with anti-γ-adaptin antibodies reaching their epitopes.

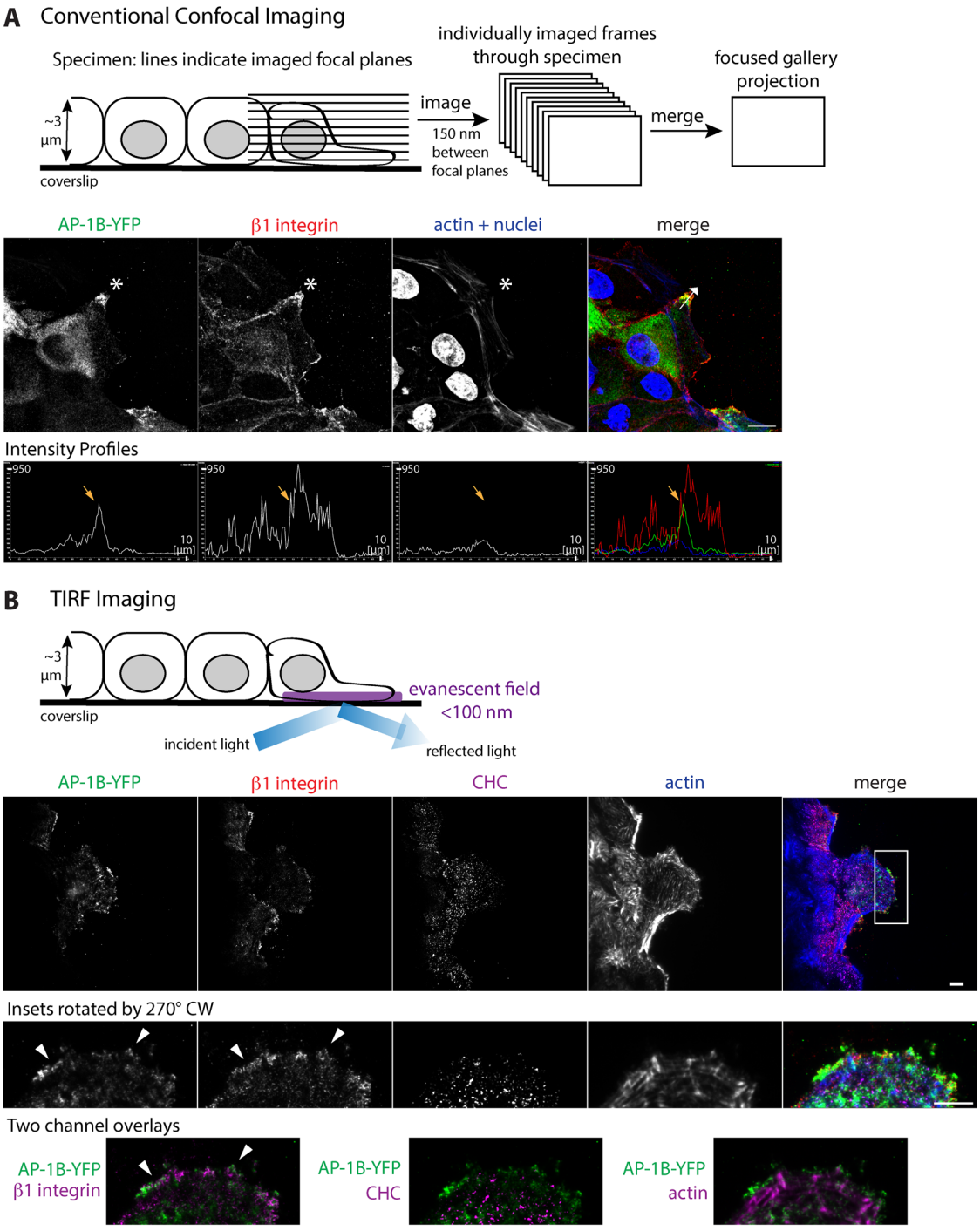

FIGURE 3: AP-1B colocalizes with β1 integrin in cell protrusions. (A) LLC-PK1::µ1B-YFP cells were grown on Matrigel-coated coverglass for 2 d. Cells were wounded and fixed 6 h later. Specimens were stained for YFP (green), β1 integrin (red), actin cytoskeleton (blue), and nuclei (blue) and analyzed by confocal microscopy as depicted in the schematic. Representative collapsed images of acquired 3D galleries are shown. Stars (*) point to the edge of a cell protrusion. Arrow in the merged image indicates the line scan position used to generate the intensity profiles. The maximum intensity was 950, and the length of the line scan arrow was 10 µm. The arrow in the line scan profiles points to the position of the peak of AP-1B fluorescence. Bar is 10 µm. (B) LLC-PK1::µ1B-YFP cells were grown in Matrigel-coated MatTek dishes for 2 d, wounded, and fixed 4–6 h later. Cells were immunolabeled for YFP (green), β1 integrin (red), CHC (magenta), and the actin cytoskeleton (blue). Specimens were imaged by TIRF microscopy and representative images are shown. Rectangle in the merged image indicates area that was cropped for zoomed-in displays (insets). Arrowheads in the insets point to the β1 integrin-positive cell edges. Two-channel overlays were generated in Photoshop. Bars are 10 µm.

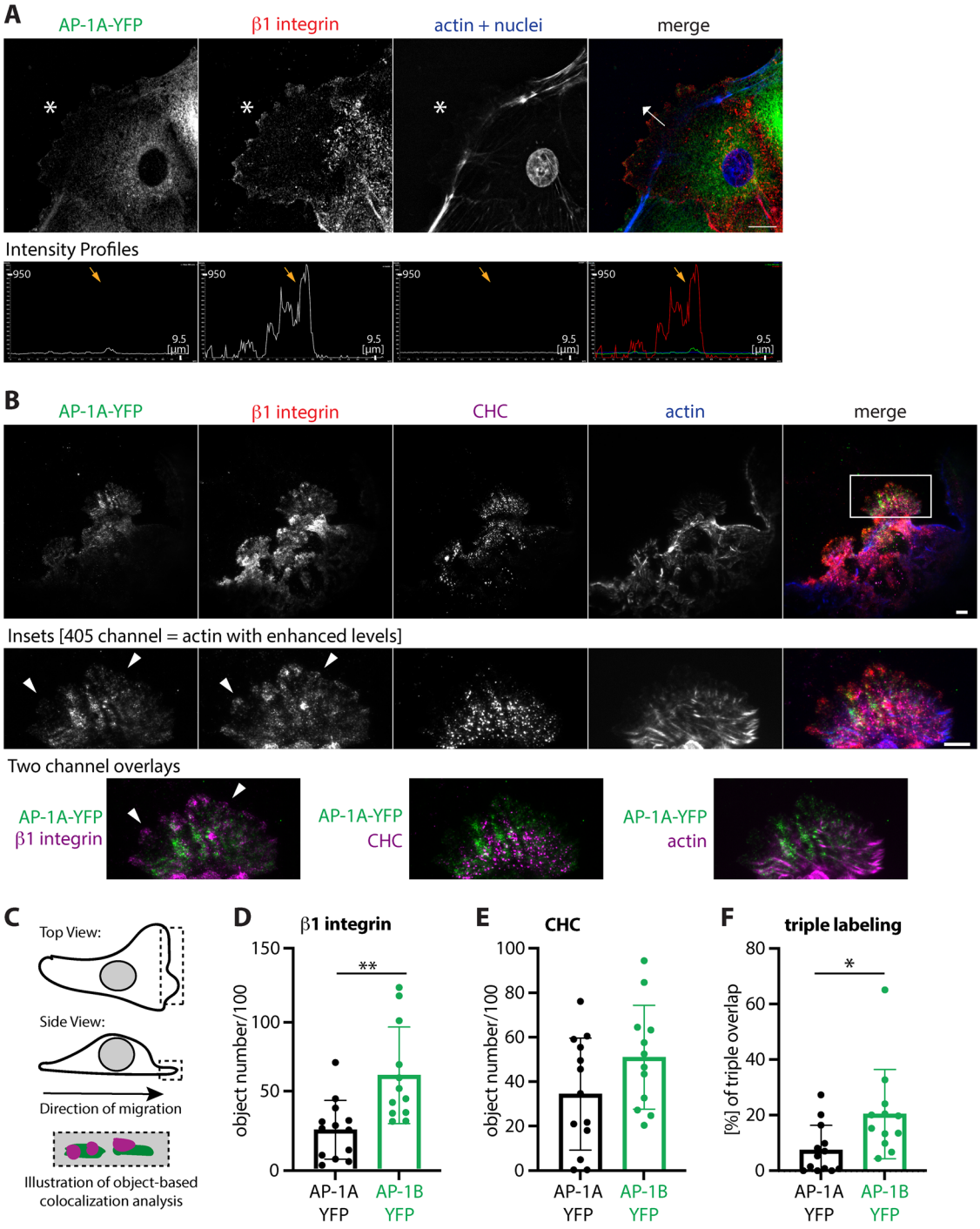

FIGURE 4: AP-1A does not colocalizes with β1 integrin. (A) LLC-PK1::μ1A-YFP cells were grown on Matrigel-coated coverglass for 2 d. Cells were wounded and fixed 6 h later. Specimens were stained for YFP (green), β1 integrin (red), actin cytoskeleton (blue), and nuclei (blue), and analyzed by confocal microscopy. Representative collapsed images of acquired 3D galleries are shown. Stars (*) point to the edge of a cell protrusion. Arrow in the merged image indicates the line scan position used to generate the intensity profiles. The maximum intensity was 1050 with the 950 position marked, and the length of the line scan arrow was a little less than 10 μm with the 9.5 μm position marked in the profiles. The arrow in the line scan profiles points to the peak fluorescence of β1 integrin. Note the absence of both AP-1A and actin fluorescent staining at the leading edge. Bar is 10 μm. (B) LLC-PK1::μ1A-YFP cells were grown in Matrigel-coated MatTek dishes for 2 d, wounded, and fixed 4–6 h later. Cells were immunolabeled for YFP (green), β1 integrin (red), CHC (magenta), and the actin cytoskeleton (blue). Specimens were imaged by TIRF microscopy and representative images are shown. Rectangle in the merged image indicates area that was cropped for zoomed-in displays (insets). Arrowheads in the insets point to the β1 integrin-positive cell edges. Two-channel overlays were generated in Photoshop. The levels for the 405 channel for the insets were enhanced in Nikon elements software before exporting the cropped images as TIF files for better appreciation of the actin staining. Bars are 10 μm. (C) Schematic

Next we sought to confirm AP-1B localization in cell protrusions in LLC-PK1::μ1B-HA cells that express HA-tagged μ1B (Fölsch *et al.*, 2001). Cells were again seeded and processed for TIRF analysis on fixed specimens. To this end, specimens were labeled for μ1B-HA/AP-1B-HA, α-adaptin/AP-2, CHC, and the actin cytoskeleton. As seen for AP-1B-YFP, AP-1B-HA was found in cell protrusions in areas that were distinct from AP-2 labeling (Figure 5B, arrowheads 1 pointing to AP–2-positive foci, arrowheads 2 pointing to AP–1B–HA-positive foci; see Supplemental Figure S2E for a larger area of shown protrusion). Object-based colocalization analysis revealed only 15.3 AP–2-positive objects but 65.8 CHC-positive objects in 100 AP–1B–HA-positive areas (Figure 5D, $P < 0.0001$). In addition, we detected 48.4 CHC-positive objects per 100 AP–2-positive fields (Figure 5E). Note that colocalization between CHC and AP-1B as well as CHC and AP-2 at the leading edges seemed underwhelming. Although colocalization is most likely underestimated, because a fully formed clathrin coat is expected to interfere with adaptor complex labeling, a lack of profound colocalization between CHC and AP-2 in TIRF has been previously observed. This was in part due to a function for CHC in lamellipodia formation that was independent of adaptor complexes and membrane trafficking (Gautier *et al.*, 2011).

In summary, AP-1B and AP-2 did not colocalize at the plasma membrane in cell protrusions during epithelial-sheet migration. As expected, both AP-1B and AP-2 colocalized to the same extent with CHC.

Super Resolution Microscopy of AP-1B in cell protrusions

To gather structural information of the AP-1B foci in cell protrusions, we performed stochastic optical reconstruction microscopy (STORM) that relies on detection of stochastic fluorophore "blinking" to obtain high-resolution images with a resolution limit of about 20 nm (van de Linde *et al.*, 2011) and thus can theoretically distinguish between labeling of vesicles or endosomes as opposed to labeling of cytoskeletal elements as illustrated in Figure 6A. Furthermore, STORM is carried out in an evanescent field like TIRF microscopy and therefore mainly detects signals originating at or in close apposition to the basal plasma membrane. For STORM imaging, LLC-PK1::μ1B-HA cells as well as LLC-PK1::μ1A-HA cells as controls were grown in monolayers on MatTek dishes coated with 1 mg/ml Matrigel. Cells were wounded and allowed to migrate before being fixed and stained with anti-HA primary antibodies followed by Alexa 647-labeled secondary antibodies. Whereas we readily detected robust STORM signals in LLC-PK1::μ1B-HA cells, we detected virtually no STORM signals in LLC-PK1::μ1A-HA cells (Figure 6B, $P < 0.0001$), in agreement with our TIRF data showing that AP-1A-YFP fails to localize to the edge of cell protrusions (compare Figure 4B). As another internal, negative control, we detected no STORM signal in LLC-PK1 cells that were negative for μ1A-HA or μ1B-HA expression (unpublished data).

Figure 6C shows a representative cell protrusion of LLC-PK1::μ1B-HA cells analyzed with STORM. There are numerous AP–1B–HA-positive signals directly at the wound edge in addition to general labeling at the basal plasma membrane of the cell protrusion. These signals were scattered, suggesting AP-1B localization in vesicles as opposed to cytoskeletal structures. Indeed, when events were clustered (5 counts, 70-nm radius to mimic vesicles), many puncta remained (about 70% of events were identified in clusters for the cell shown). This was true for ~90% of analyzed cells.

Thus STORM analysis of LLC-PK1::μ1B-HA cells provides further evidence that AP-1B may be present in vesicles located close to or at the basal plasma membrane during cell migration.

AP-1B localizes to vesicles and pits at the plasma membrane

As a clathrin adaptor, AP-1B may facilitate the generation of clathrin-coated vesicles, and indeed immunoisolation of AP-1B vesicles coprecipitated CHC (Fölsch *et al.*, 2003, and Supplemental Figure S1C). Thus, to further clarify AP-1B's localization with relation to the plasma membrane, we performed immunoelectron microscopy (immuno-EM) to investigate if AP-1B may be localized either in vesicles that invaginate from the plasma membrane or to pits that represent more flat structures that may or may not progress into forming vesicles (Wang *et al.*, 2020). We chose LLC-PK1::μ1B-HA cells for these studies, because we previously had reliable results with immunogold labeling of AP-1B-HA (Fölsch *et al.*, 2001, 2003). To enhance labeling efficiency and reduce steric hindrance of the gold-labeled secondary antibodies during pre-embedding labeling, we used nanogold (1.4 nm)-labeled secondary antibodies followed by a silver enhancement reaction during which silver precipitates around the gold particles. The precipitates present as amorphous, high-contrast structures in the EM images.

We readily found numerous AP–1B–HA-labeled structures that were in close apposition to the plasma membrane in migrating cells indicative of pits and forming vesicles at the plasma membrane (Figure 6D). A vesicle coated with AP-1B that is seemingly invaginating from the plasma membrane is indicated by arrow 1, whereas a pit coated with AP-1B is indicated by an arrow labeled 2 in Figure 6D.

Next we sought to determine labeling densities at the plasma membrane. To this end we took into consideration that AP-1B is a clathrin adaptor (Fölsch *et al.*, 1999; Deborde *et al.*, 2008), whose canonical recruitment of clathrin results in the formation of clathrin-coated vesicles (Fölsch *et al.*, 2003, and Supplemental Figure S1C). The diameter of clathrin-coated vesicles typically ranges from about 75 to 130 nm (Pearse and Robinson, 1984; Kural *et al.*, 2012). Thus, to determine labeling densities of AP-1B pertaining to invaginating vesicles and pits at the surrounding (lateral) plasma membrane, we determined total amounts of label as well as label within a narrow range of 50 and 100 nm from the surrounding membrane of whole cells at the wound edge imaged with a dark field detector. With a dark field detector, the silver precipitates appear white in a dark background allowing for easy detection (Supplemental Figure S3A). LLC-PK1::μ1A-HA cells were processed and imaged as control (Supplemental Figure S3B). Of the total signal, 3% of AP-1B-HA label was within 100 nm and 1.4% was within 50 nm of the surrounding membrane in comparison to only 1.6 and 0.5% of total AP-1A-HA label (Figure 6E, left graphs). Because cell shape varied (compare Supplemental Figure S3), we also determined label within 250 and 500 nm of the surrounding plasma membrane and calculated labeling densities in these areas. Within these areas, we again found that

illustration of object-based colocalization analysis. (D–F) Object-based colocalization analysis of β1 integrin-positive objects (D) and CHC-positive objects (E) in AP-1A-YFP or AP–1B–YFP-positive areas as well as measurement of fields with all three markers (F) was performed with Nikon Elements software as described in *Materials and Methods* and as depicted in C. We analyzed 13 well-formed protrusions of LLC-PK1::μ1A-YFP cells from three independent experiments and 12 well-formed protrusions of LLC-PK1::μ1B-YFP cells from three independent experiments. $^{**}P < 0.003$; $^{*}P < 0.02$.

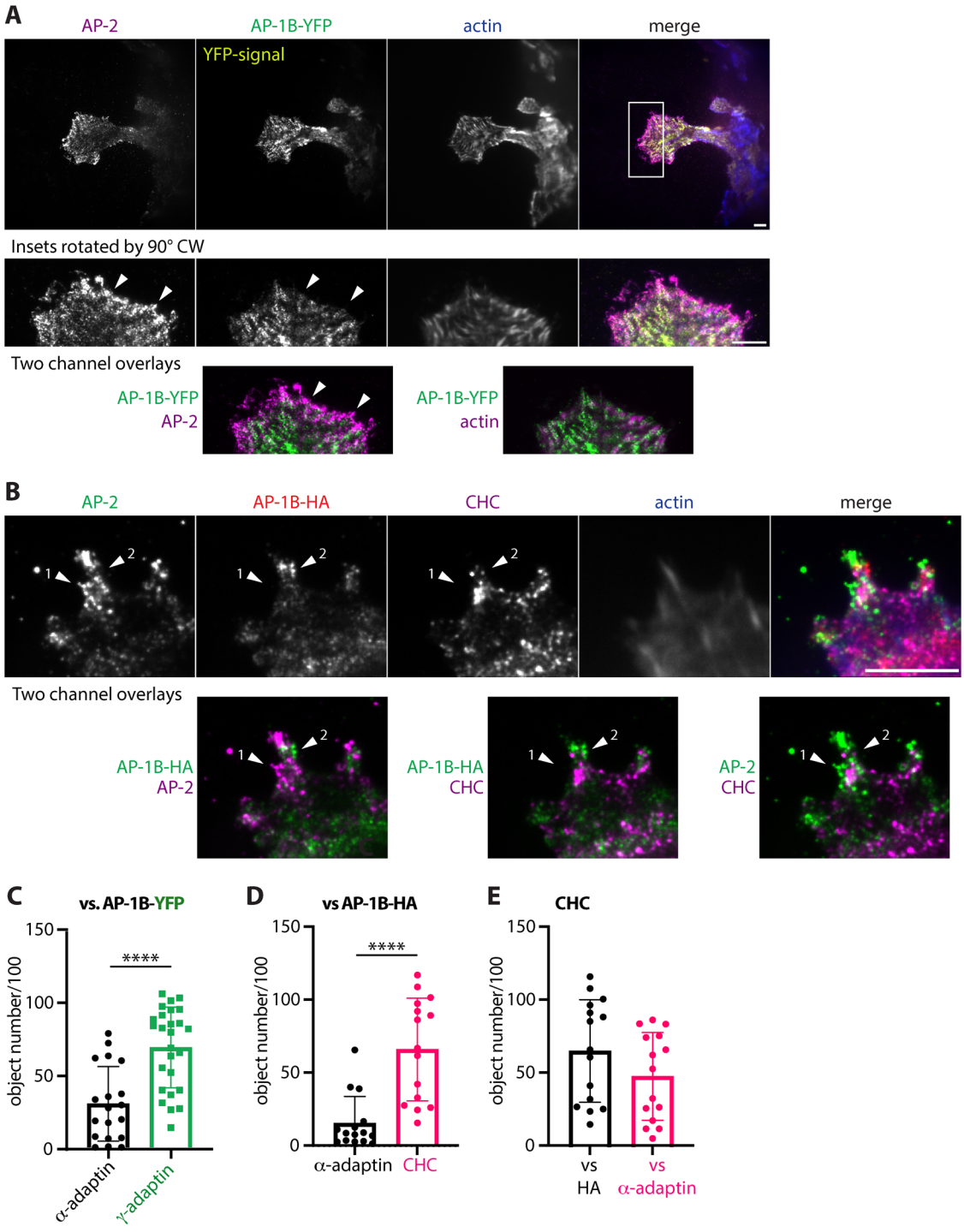

FIGURE 5: AP-1B does not colocalize with AP-2. LLC-PK1 cell lines stably expressing μ1B-YFP or μ1B-HA were grown in Matrigel-coated MatTek dishes for 2 d, wounded, and fixed 4-6 h later. (A) LLC-PK1::μ1B-YFP cells were immunolabeled for AP-2 (magenta) and the actin cytoskeleton (blue). AP-1B-YFP was imaged directly via the YFP signal. Specimens were imaged by TIRF microscopy and representative images are shown. Arrowheads in the insets point to AP–2-positive foci that are devoid of AP-1B-YFP labeling. Rectangle in the merged image indicates the area that was cropped for zoomed-in displays (insets). (B) LLC-PK1::μ1B-HA cells were immunolabeled for AP-2 (green), μ1B-HA/AP-1B-HA (red), CHC (magenta), and the actin cytoskeleton (blue). Specimens were imaged by TIRF microscopy and representative images are shown. Arrowhead 1 points to AP–2-positive foci and arrowhead 2 points to AP–1B–HA-positive foci. (A and B) Two-channel overlays were generated in Photoshop. Bars are 10 μm. (C–E) Object-based colocalization analyses were performed with Nikon Elements software as described in *Materials and Methods* (see also Figure 4C for a schematic illustration). (C) Results of object-based colocalization analysis of α–adaptin/AP–2-positive and γ–adaptin-positive objects in μ1B–YFP/AP–1B–YFP-positive areas. We analyzed 19 well-formed protrusions of LLC-PK1::μ1B-YFP cells from three independent experiments to score colocalization with α-adaptin and 26 well-formed protrusions of LLC-PK1::μ1B-YFP cells from three independent experiments to score colocalization with γ-adaptin. (D and E) Results of object-based

the labeling density of AP-1B-HA at the lateral plasma membrane was significantly higher than the labeling density of AP-1A-HA (Figure 6E, right graphs). This confirms the immunofluorescence data acquired by either conventional confocal microscopy or TIRF imaging as shown in Figures 3 and 4. Importantly, we detected no label in cells that were negative for HA-tagged AP-1s (Supplemental Figure S3C). Note that with EM technology, it is impossible to discern how closely apposed labeling within the cell body is to the basal plasma membrane. Thus, although statistically significant, the amount of AP-1B-label at the plasma membrane is most likely underestimated, because we could only determine labeling density at the surrounding, lateral plasma membrane but not at the basal plasma membrane. This is in contrast to TIRF, where only label at or in close apposition to the basal plasma membrane is detected, allowing us to discern AP-1B label also at or close to the basal plasma membrane.

Taken together, our diverse imaging approaches ranging from conventional confocal microscopy, TIRF, and STORM imaging to immuno-EM all showed consistent labeling of AP-1B at or close to the plasma membrane with significantly less labeling of AP-1A in the same area. AP-1B labeling in close apposition to the plasma membrane in cell protrusions is a novel finding.

AP-1B expression is lost in metastatic cancer cells

Because AP-1B decreased cell migration speeds and localized close to or at the plasma membrane in cell protrusions during migration, we wondered if epithelial-derived, highly migratory cancer cells may have reduced levels of AP-1B. Therefore, we measured μ1B transcript levels by quantitative real-time reverse transcription PCR (qRT-PCR) in various human cell lines. Indeed, we found μ1B transcripts in normal breast epithelial cells MCF10A and 76NTER, as well as HBE and Caco-2 cells. However, we detected virtually no μ1B transcripts in the triple-negative breast cancer cell line MDA-MB-231 and the cervical cancer HeLa cell line (Figure 7A). This is in agreement with an earlier Northern blot analysis that showed expression of μ1B in Caco-2 cells and absence of μ1B in HeLa cells as well as fibroblast cell lines (Ohno *et al.*, 1999). In contrast, ARH transcripts were found in all tested cell lines (Figure 7B).

Search for the μ1B gene (ap1m2) in the Cancer Dependency Map (depmap.org, ap1m2 search run in the second quarter of 2020 = 20Q2) revealed about 20 epithelial-derived carcinomas with missense or nonsense mutations in μ1B (Mutations Public 20Q2). Moreover, expression analysis of RNASeq data showed numerous epithelial-derived lines with lower to no expression of μ1B (Expression Public 20Q2). This is in line with earlier reports that more than 80% of kidney cancers arose in proximal kidney tubules (Holthofer *et al.*, 1983; Gu *et al.*, 1991; Martensson *et al.*, 1995) that naturally lack μ1B expression (Schreiner *et al.*, 2010). Moreover, μ1B expression was down-regulated in mouse models for colon cancer (Mimura *et al.*, 2011). Thus, a lack of μ1B expression may be another hallmark of metastatic cancer.

DISCUSSION

Using wound healing assays we showed that AP-1B expression and ARH expression in AP–1B-positive epithelial cells slowed collective cell migration. We further established β1 integrin as a cargo protein that is sorted to the basolateral membrane by AP-1B and ARH. During collective cell migration, we found AP-1B colocalized with β1 integrin and clathrin at the plasma membrane in cell protrusions in areas that were not occupied by AP-2. STORM analysis was consistent with AP-1B's presence in vesicles at or close to the basal plasma membrane. Indeed, EM analysis showed AP-1B localizing in coated pits and vesicles at the plasma membrane in migrating cells. Taken together, this study establishes localization of AP-1B at the plasma membrane in cell protrusions and implicates a regulatory role for AP-1B in cell migration. This novel function of AP-1B is not shared by AP-1A.

How does AP-1B influence migration speed? We found AP-1B colocalized with β1 integrin, and integrins regulate various cellular processes including cell spreading, formation of focal adhesions, and cell migration (Moreno-Layseca *et al.*, 2019). Therefore, AP-1B's role in migration is most likely linked to β1 integrin either in a structural or in a membrane trafficking function. Recently, CHC was implicated in Scar/Wave-mediated lamellipodia formation (Gautier *et al.*, 2011). This role was uncoupled from CHC's role in membrane trafficking and independent of clathrin light chain (Gautier *et al.*, 2011). Moreover, AP-2 was shown to regulate adhesion in a 3D matrix independently from CHC by forming tubelike lattices around collagen fibers (Elkhatib *et al.*, 2017). Thus it might be that AP-1B has a similar structural function in cell migration and lamellipodia formation. Structural functions of AP-2 and AP-1B might further explain the relatively low level of colocalization between AP-2 and CHC as well as AP-1B and CHC in cell protrusions. Indeed, previous studies also noticed a lack of colocalization between AP-2 and CHC at cell edges (Gautier *et al.*, 2011). However, positive roles in lamellipodia formation are typically associated with an increase in migration speed (Gautier *et al.*, 2011; Paul *et al.*, 2015; Moreno-Layseca *et al.*, 2019) and thus cannot explain why AP-1B expression decreased migration speed.

It is further possible that AP-1B's role in cell protrusions is to recycle and deliver β1 integrin to the leading edge (Figure 7C, possibility 1) Exocytosis). For example, family members of the monomeric clathrin adaptors Golgi-localized gamma-ear containing proteins (GGAs) have been implicated in integrin recycling. Indeed, GGA3 was shown to regulate β1 integrin trafficking to the cell periphery and depletion of GGA3 led to reduced cell migration (Ratcliffe *et al.*, 2016). Furthermore, GGA2 together with its effector Rab13 were shown to promote recycling of β1 integrin and silencing of GGA2 or Rab13-reduced migration speed (Ratcliffe *et al.*, 2016; Sahgal *et al.*, 2019). Finally, GGA1 was found together with clathrin in "gyrating" structures at the basal membrane during migration that were suggested to be part of an endosomal recycling compartment and involved in rapid recycling (Zhao and Keen, 2008). Consisting with a role in recycling, depletion of GGA1 also reduced migration speeds (Ratcliffe *et al.*, 2016). Thus, even though AP-1B may play its "normal" role in recycling during migration, this cannot explain why its depletion enhanced migration. Moreover, we found AP-1B label close to the cell periphery. Typically, one would expect vesicle coats to be shed close to the fusion site, indicating that this label may not represent exocytic vesicles. Indeed, using TIRF microscopy, exocytosis was observed all over the basal plasma membrane, but fusion of exocytic carriers was excluded within 1–2 μm from the cell edge

colocalization analysis of α-adaptin/AP-2 and CHC-positive objects in μ1B–HA/AP–1B–HA-positive areas (D) as well as measurement of CHC-positive objects in α–adaptin/AP–2-positive areas plotted against CHC in μ1B–HA/AP–1B–HA-positive areas (E). We analyzed 15 well-formed protrusions of LLC-PK1::μ1B-HA cells from three independent experiments. ****$P < 0.0001$.

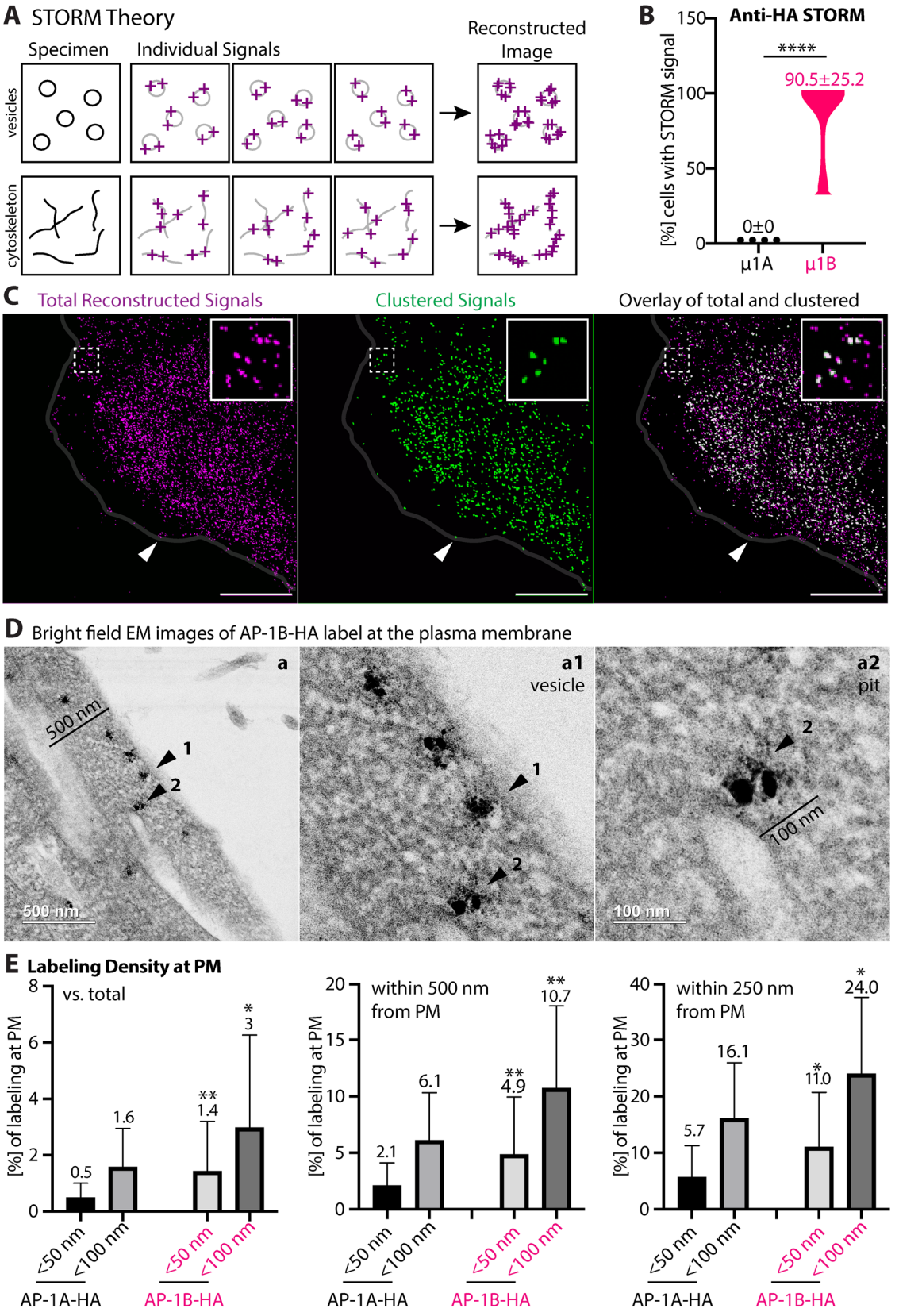

FIGURE 6: AP-1B localizes in vesicles at the plasma membrane. (A) Schematic illustration of expected STORM results if vesicles are imaged in contrast to the cytoskeleton. Stochastic fluorophore blinking over many frames is reconstructed into a STORM image. (B and C) LLC-PK1::µ1B-HA cells were grown in Matrigel-coated MatTek dishes for 2 d. Cells were fixed 1.5 h after wounding and stained with anti-HA antibodies followed by Alexa 647-labeled secondary antibodies. STORM buffer was added and specimens were imaged using STORM followed by processing using Nikon Elements software as described in *Materials and Methods*. We recorded a total of 21 LLC-PK1::µ1B-HA cells in seven independent

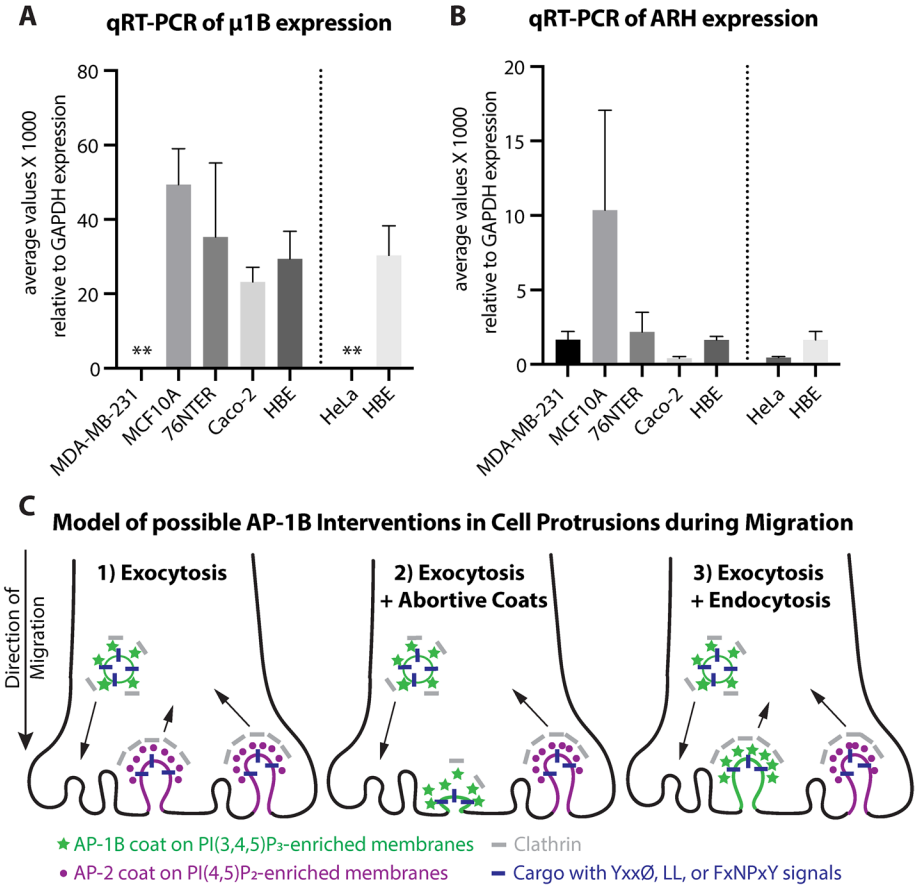

FIGURE 7: AP-1B expression is lost in highly metastatic cancer cells. (A and B) qRT-PCR was performed using one set of primers specific for human µ1B (A) or human ARH (B). Transcript levels from three independent experiments each done in triplicates were plotted in relation to GAPDH transcript levels. The dotted line separates independently run triplicates comparing µ1B transcripts among MDA-MB-231, MCF10A, 76NTER, Caco-2, and HBE cells as well as HeLa and HBE cells. Error bars indicate SD. $^{**}P < 003$ for all cell lines vs. HeLa and MDA-MB-231 cells with exception of the pair 76NTER and MDA-MB-231 where P was 0.0372, which is still considered statistically significant. (C) Model depicting three possible scenarios of putative AP–1B-mediated events in cell protrusions: 1) depicts a role for AP-1B solely in exocytosis, 2) considers an additional role in forming abortive coats that may interfere with endocytosis, and 3) considers a role for AP-1B in endocytosis alongside AP-2.

in migrating fibroblasts (Schmoranzer *et al.*, 2003). A similar exclusion of fusion in peripheral zones was observed in migrating PtK_2 kidney epithelial cells (Toomre *et al.*, 2000).

Does AP-1B form clathrin coats at the plasma membrane during cell migration? Finding AP-1B label in close apposition to the plasma membrane in part colocalizing with CHC certainly suggests that, but does that mean AP-1B facilitates endocytosis (Figure 7C, 3) Exocytosis + Endocytosis)? Alternatively, AP-1B may form coats that are aborted shortly after forming without generating endocytic carriers (Figure 7C, 2) Exocytosis + Abortive Coats; Wang *et al.*, 2020). In this latter scenario, AP-1B would competitively occupy binding sites for AP-2 thus lowering the net rate of AP-2-mediated endocytosis of β1 integrin. Indeed, previous studies showed that inhibition of endocytosis decreases migration speed by slowing focal adhesion turnover rates (Ezratty *et al.*, 2009; Fletcher *et al.*, 2012). However, it is also possible that AP-2 as well as AP-1B facilitate endocytosis in cell protrusions. To this end, one could speculate that while AP-2 internalizes mature focal adhesion, AP-1B may internalize nascent adhesions. Nascent adhesions are mainly found at the very end of cell protrusions (Winograd-Katz *et al.*, 2014). They are not yet engaged with actin, but may develop into mature focal adhesions over time. Mature focal adhesions are marked by their attachment to actin stress fibers (Winograd-Katz *et al.*, 2014; Moreno-Layseca *et al.*, 2019). Only mature focal adhesions are generating traction forces and thus forward movement during cell migration (Moreno-Layseca *et al.*, 2019). By internalizing nascent adhesion complexes, AP-1B could

experiments. The percentage of cells at the wound edge that expressed AP-1B-HA and gave positive STORM signals was calculated per experiment and averaged as presented in the violin blot in B. No STORM signals were detected in LLC-PK1::µ1A-HA cells (four independent experiments). The cell shown in C had 19,639 out of 21,380 molecules identified as specific signals. 13,654 molecules were identified in clusters of at least five counts in a 70-nm radius. Arrowhead points to a clustered event at the edge of the cell protrusion. Bars are 10 µm. (D) LLC-PK1::µ1B-HA cells were wounded 2 d after seeding in Matrigel-coated MatTek dishes. After ~7 h, cells were fixed and processed for pre-embedding labeling with anti-HA primary and 1.4-nm gold-labeled secondary antibodies, followed by a silver enhancement reaction for 10 min, and processed for EM as described in *Materials and Methods*. Bright field images were acquired with the phase contrast bright field (TE) detector attached to the EM. Zoomed-in images in panel a were either cropped from the TIF file (a1) or directly imaged at higher resolution (a2). Bars are as indicated (500 nm for a; 100 nm for a2). Because a1 was cropped out of an existing TIF file, it has no scale bar. Numbered arrows point to the same regions in the individual images that are positive for AP-1B-HA labeling in coated vesicles (arrowhead 1) or pits (arrowhead 2) originating at the plasma membrane. (E) To determine labeling density at the plasma membrane (PM) EM images were analyzed using ImageJ software as described in *Materials and Methods* to determine total counts. We then counted individual labels within 50, 100, 250, and 500 nm from the PM. Data are expressed as percentages of label that occurred in close proximity (<50 and <100 nm) to the PM in relation to the total counts (left graph) or within a range of 500 or 250 nm from the PM (middle and right graphs). We analyzed a total of 34 AP-1A-HA and 25 AP-1B-HA expressing LLC-PK1 cells. To determine statistical significance, similar data sets between AP-1A-HA and AP-1B-HA expressing cells were compared (e.g., <50 nm/total AP-1A-HA vs. <50 nm/total AP-1B-HA and so forth). Error bars indicate SD. $^{**}P < 0.006$; $^{*}P < 0.04$.

lower the amount of mature focal adhesions that can form and thus lower migration speed. This would be consistent with AP-1B's observed partial localization at the very edge of cell protrusion in a staining pattern that was largely distinct from actin labeling. Future studies are directed at distinguishing between these scenarios.

Recruitment of AP-1B to the plasma membrane in cell protrusions was probably facilitated by an enrichment in $PI(3,4,5)P_3$ found at these sites (Franca-Koh *et al.*, 2007; Fields *et al.*, 2010), and colocalization with β1 integrin was most likely bridged via ARH. Furthermore, we predict that Arf6 may also play a role in recruiting AP-1B into cell protrusions (Santy and Casanova, 2001; Shteyn *et al.*, 2011). Currently, we are unable to easily and reliably costain for AP-1B and $PI(3,4,5)P_3$ and Arf6, as well as ARH during cell migration due to low transfection efficiencies. To this end, new stable cell lines would be required, which is beyond the scope of this study. Regardless, AP-1B did not colocalize with AP-2. Indeed, it is well known that membrane recruitment of AP-2 is strictly dependent on $PI(4,5)P_2$ and thus AP-2 should be absent from areas that are enriched in $PI(3,4,5)P_3$ (Collins *et al.*, 2002). In contrast to AP-1B and AP-2, we found AP-1A largely absent from focal adhesions and the plasma membrane, most likely because AP-1A is normally recruited onto PI(4)P-positive membranes at the TGN and endosomes (Wang *et al.*, 2003).

In fully polarized cells, AP-1B is not recruited to the plasma membrane at steady state although the basolateral domain is enriched in $PI(3,4,5)P_3$ (Gassama-Diagne *et al.*, 2006; compare μ1B-YFP/AP-1B-YFP fluorescence in Figure 1F). Perhaps Arf6 is not activated at the basolateral membrane and therefore AP-1B may not be recruited. Indeed, the PH-domain of Grp1 that bound both $PI(3,4,5)P_3$ and activated Arf6 (Di Paolo and De Camilli, 2006; DiNitto *et al.*, 2007) localized in REs and membrane ruffles, but not at the lateral membranes (Fields *et al.*, 2010). Moreover, whereas Arf6 facilitated endocytosis from the apical membrane (Altschuler *et al.*, 1999), it played no role in endocytosis from the basolateral membrane of fully polarized MDCK cells (Boulant *et al.*, 2011), consistent with an absence of active Arf6 at this site.

The fold change in migration speeds we observed in wound healing assays ranged between 20 and 40% both in gain-of-function (e.g., LLC-PK1 cell lines) or loss-of-function (e.g., depletion in MDCK cells) scenarios. These fold changes are in line with other migration studies done in epithelial cells. For example, depletion of E-cadherin in Caco-2 cells reduced migration speeds by approximately 50% (Hwang *et al.*, 2012), and cleavage of the v-SNARE Vamp3 in MDCK cells stably expressing tetanus neurotoxin resulted in a reduction in velocity from about 17 μm/h to 8 μm/h (Proux-Gillardeaux *et al.*, 2005). Vamp3 is needed for endosomal membrane trafficking, integrity of REs, and AP–1B-facilitated exocytosis in epithelial cells (Galli *et al.*, 1994; Daro *et al.*, 1996; Fields *et al.*, 2007).

E-cadherin is a major adherens junction protein with a highly conserved dileucine sorting signal (= LL-motif) for delivery to the basolateral membrane (Miranda *et al.*, 2001). Although basolateral sorting does not depend on AP-1B per se (Miranda *et al.*, 2001; Gravotta *et al.*, 2007), AP-1B is necessary for efficient basolateral delivery of E-cadherin (Ling *et al.*, 2007), and parental LLC-PK1 cells deliver less E-cadherin to the basolateral membrane than LLC-PK1::μ1B cells that express AP-1B (Ling *et al.*, 2007). Based on these data, it is surprising that lack of AP-1B expression led to an increase in migration speed, because epithelial-sheet migration is positively correlated with E-cadherin levels at the basolateral membrane (Hwang *et al.*, 2012): the more E-cadherin, the faster the speed. Thus, the positive effect that absence of AP-1B has on epithelial-cell migration may in part be countered by lower amounts of E-cadherin at the basolateral membrane. This may explain at least in part why depletion of ARH in AP–1B-expressing cells resulted in a greater change (~80% increase in speed) than depletion of AP-1B expression in MDCK cells. Unlike AP-1B, ARH only affects basolateral sorting of cargos with FxNPxY signals, but not cargos with YxxØ and LL-based sorting signals (Kang and Fölsch, 2011) and is thus not necessary for delivery of E-cadherin to the basolateral membrane. Alternatively, ARH-independent functions of AP-1B in, for example, membrane recycling to the leading edge may lower the overall negative effect of AP-1B on migration and thus depletion of AP-1B may result in a lower net increase in speed as opposed to ARH depletion.

Curiously, depletion of ARH in AP–1B-negative cells resulted in slower cell migration (Ezratty *et al.*, 2009). In fact, depletion of AP-2, ARH, and Dab-2 all inhibited focal adhesion turnover and resulted in decreased migration (Ezratty *et al.*, 2009). Why then does ARH depletion in AP–1B-expressing cells enhance migration? It should be noted that unlike AP-2 that can cooperate with ARH, Dab-2, and numb (Traub, 2003), AP-1B can only cooperate with ARH (Kang and Fölsch, 2011). Therefore, ARH would be needed to target AP-1B to β1 integrin at the plasma membrane. The increase in migration speed after ARH depletion in AP–1B-positive cells may thus be a reflection of the inhibitory effect of AP-1B. This would also imply that ARH cooperates with AP-1B in controlling cell migration.

What are the physiological consequences of AP-1B expression in polarized epithelial cells? When we first described AP-1B, we noticed that re-expression of μ1B in LLC-PK1 cells had a profound effect on monolayer appearance. Whereas LLC-PK1::μ1B cell grew in monolayers, LLC-PK1::μ1A cells grew on top of each other (Fölsch *et al.*, 1999). Indeed, μ1B knockout mice developed intestinal epithelial cell hyperplasia that was attributed in part to mislocalization of E-cadherin and activation of the β-catenin/Tcf4 complex (Hase *et al.*, 2013). Curiously, β1 integrin, unlike other integrins, is localized not only to the basal but also to the lateral surface (compare Figure 1). Further, it was shown that β1 integrin facilitates cell–cell adhesion between keratinocytes and is needed for the invasive behavior of squamous cell carcinomas (Larjava *et al.*, 1990; Brockbank *et al.*, 2005). Thus at steady state, AP-1B may also aid in preventing abnormal growth by restricting β1 integrin at the basolateral membrane in addition to regulating E-cadherin (Hase *et al.*, 2013). In the absence of AP-1B, β1 integrin is missorted to the apical membrane (compare Figure 1), most likely aided by galectin-3 (Hönig *et al.*, 2018). In highly metastatic cancer cells that lost expression of AP-1B (compare Figure 7), apically expressed β1 integrin could potentially help the survival of cells that are extruded apically from epithelial monolayers by promoting cell–cell adhesion at the apical membrane (Larjava *et al.*, 1990). During cell migration, apically localized β1 integrin might facilitate intercalation of cells when wound edges close potentially leading to abnormal growth (Brockbank *et al.*, 2005). Along these lines, histological studies suggested that > 80% of kidney cancers arose from proximal tubules that lack AP-1B expression (Holthofer *et al.*, 1983; Gu *et al.*, 1991; Martensson *et al.*, 1995; Schreiner *et al.*, 2010) implying AP-1B as an anticancer agent. This study continues shedding light on the underlying molecular mechanisms.

MATERIALS AND METHODS

Antibodies and labeling dyes

Rabbit anti-CHC (ab21679), rabbit anti-GFP (ab290), goat anti-GFP (ab6673), rabbit anti-α-adaptin (ab189995), and rabbit anti-γ-adaptin (ab220251), as well as CytoPainter Phalloidin-iFluor 405 (ab176752), were purchased from Abcam. Mouse anti-β1 integrin (MEM-101A) was purchased from Novus Biologicals, mouse anti-HA (16B12) from Covance, and mouse anti-γ-adaptin (100/3) from

Sigma. Hybridomas producing antibodies against LDL receptor (C7) were purchased from the American Type Culture Collection. Unlabeled, generic goat anti-rabbit IgG antibodies were purchased from Zymed. A polyclonal antibody cross-reacting between μ1A and μ1B was a kind gift from Linton Traub (University of Pittsburgh, Pittsburgh, PA).

Secondary antibodies labeled with Alexa dyes donkey anti-mouse Alexa 647, donkey anti-mouse Alexa 568, goat anti-mouse Alexa 488, donkey anti-goat Alexa 680, and donkey anti-goat Alexa 488 were purchased from Molecular Probes/Thermo Fisher Scientific. Donkey anti-mouse IRDye 800CW and donkey anti-rabbit IRDye 680RD antibodies were purchased from Li-Cor. Donkey anti-rabbit Cy5 antibodies, and peroxidase–conjugated goat anti-mouse and goat anti-rabbit antibodies were from Jackson ImmunoResearch. Goat anti-mouse antibodies labeled with 1.4-nm colloidal gold as well as HQ Silver enhancement kit were from Nanoprobes. DAPI solution was purchased from BD Biosciences.

Cell culture

All cells were grown at 37°C in the presence of 5% CO_2. Their respective media were, in general, supplemented with 2 mM L-glutamine, 0.1 mg/ml penicillin/streptomycin, and 0.01 mg/ml ciprofloxacin. LLC-PK1 cells stably expressing μ1A, μ1B, μ1A-HA, μ1B-HA, μ1A-YFP, or μ1B-YFP were maintained in αMEM (5% fetal bovine serum [FBS]) containing 1 mg/ml geneticin. MDCK, and HBE cells were grown in MEM (5% FBS). HeLa cells were maintained in DMEM (10% FBS), MDA-MB-231 cells were maintained in αMEM (10% FBS), and Caco-2 cells were grown in DMEM (20% FBS) supplemented with 0.1 mM nonessential amino acids, 1 mM sodium pyruvate, and 10 μg/ml transferrin. MCF10A and 76NTER cells were maintained in DMEM/F12 medium (5% horse serum) supplemented with 20 ng/ml EGF, 0.5 mg/ml hydrocortisone, 100 ng/ml cholera toxin, 10 μg/ml insulin, and 0.1 mg/ml penicillin/streptomycin. HBE and Caco-2 cells were maintained on coated surfaces. To prepare the coating solution, LHC basal medium was supplemented with 10 mg/ml bovine serum albumin (BSA), 3 mg/100 ml bovine collagen I, and 1 mg/100 ml fibronectin.

For wound healing assays, cells were seeded at densities ranging from 9 to 11 × 10^5 cells onto 22 × 22-mm coverglass placed in 35-mm dishes (confocal analysis) or into MatTek dishes (35 mm with 14-mm microwell No #1.5 coverglass for BioStation, fixed TIRF microscopy, STORM, and EM analysis) typically 2 d prior to wound healing assays such that cells formed monolayers without being overgrown. Coverglass was acid washed and coated with 1 mg/ml Matrigel. Cell monolayers were scratched with a p200 tip to wound them, followed by two washes in growth media. Cells were typically fixed 4–6 h after wounding (1.5 h after wounding for STORM). Live imaging using the BioStation typically started 0.5 to 1 h after wounding.

To monitor polarized sorting of β1 integrin, we seeded 4 × 10^5 cells on 12-mm filter supports (0.4-μm pore size; Corning) and cultured them for 4 d with changes of the medium in the basolateral chamber daily. LLC-PK1 cells were typically put on a rocker platform and rocked slowly and continuously for about 3 d prior to fixation. HBE cells were seeded on filter supports that were coated with 1 mg/ml Matrigel.

Cloning, retroviruses, and gene knockdown

The internal YFP-tags in μ1A and μ1B were introduced between amino acids 230 and 231 using PCR at the exact same position into which we previously introduced HA-tags (Fölsch *et al.*, 2001). We first amplified N-terminal fragments (amino acids 1–230) of μ1A and μ1B with flanking *Eco*RI at the N-terminus and *Xho*I and *Cla*I restriction sites at the C-terminus using the following primer pairs: 5′-GCGC GAATTC ATG TCC GCC TCG GCT GTC TTC ATT-3′ and 5′-GCGC ATCGAT CTCGAG TGA TTT GTT CTT GCT GCG GCC AGT-3′ for human μ1B and 5′-GCGC ATCGAT CTCGAG TGA CTT GCT CTT CCC TCG GCC TGT-3′ and 5′-GCGC GAATTC ATG TCC GCC AGC GCC GTC TAC GTA-3′ for mouse μ1A. We used these fragments to exchange them with the N-terminal parts including the HA tag of our previous constructs through a simple cut-and-paste approach. We then amplified enhanced YFP using pEYFP-C1 as a template and the following primers: 5′-GCGC CTCGAG ATGGT-GAGCAAGGGCGAGGAG-3′ and 5′-GCGC ATCGAT CTTGTA-CAGCTCGTCCATGCC-3′. EYFP was introduced between *Xho*I and *Cla*I sites in μ1A and μ1B using cut-and-paste technology. Constructs were confirmed through sequencing; no errors were found. The pCB6 vector backbones now containing μ1A-YFP and μ1B-YFP were subsequently used to generate stable cell lines.

The shRNAmir constructs in the lentiviral pGIPZ vector targeting human ARH (CGCTTGGCACTTTAAAGCATTATAGTGAAGCCACA-GATGTATAATGCTTTAAAGTGCCAAGC) and human GAPDH were described previously (Nokes *et al.*, 2008; Kang and Fölsch, 2011). The retroviral constructs in RVH1 specifically targeting canine μ1B (CCCCGCAGTCAGTGGCCAATGGTTTCAAGAGAACCATTGGC-CACTGACTGCTTTTTGGAAA) and scrambled control were as previously described (Anderson *et al.*, 2005). HBE cells stably depleted of ARH or GAPDH as well as MDCK cells depleted of μ1B or scrambled control were generated by infecting HBE or MDCK cells with respective retroviruses exactly as previously described (Anderson *et al.*, 2005; Pigati *et al.*, 2013). Cells were maintained in growth media with 12 μg/ml puromycin. Depletion of ARH or μ1B mRNAs was monitored using RT-PCR.

RT-PCR and qRT-PCR

RNA was typically isolated from confluent monolayers of cells seeded in 10-cm plates using the direct-zol RNA miniprep kit from Zymo Research; 1.5 μg of purified RNA was used for reverse transcription using Superscript III enzyme (Invitrogen). Reverse-transcribed RNA was subsequently used for conventional RT-PCR or qRT-PCR using Taq polymerase. qRT-PCR was performed using the light Cycler 480 II real-time PCR machine from Roche and SYBR green detection.

(q)RT-PCR primers to amplify human ARH were N-terminal primer 5′-ATCGTGGCTACAGCTAAGGC-3′ and C-terminal primer 5′-GCCT-TAGCTGTAGCCACGAT-3′, human μ1B was amplified using N-terminal primer 5′-TCCCTCCCCGACTCCTAAGT-3′ and C-terminal primer 5′-GTGGCCACCAAGTAGAGGTT-3′, and human GAPDH was amplified using N-terminal primer 5′-ACAGTCAGCCGCATCTTCTTT-3′ and C-terminal primer 5′-CAATACGACCAAATCCGTTGACT-3′. Canine ARH was amplified using N-terminal primer 5′-TTGCCT-ACATTGCACAGAGC-3′ and C-terminal primer 5′-CTTGGACACC-TGCCAAAACT-3′, canine μ1B was amplified using N-terminal primer 5′-TGGGGTCAAGTTTGAGATCC-3′ and C-terminal primer 5′-GCCCGGTAACCTCTTTTCTC-3′, and canine GAPDH was amplified using N-terminal primer 5′-GCCAAGAGGGTCATCATCTC-3′ and C-terminal primer 5′-AGGAGGCATTGCTGACAATC-3′.

qRT-PCRs (Figure 7) were run three times in triplicates on independently isolated RNA samples and analyzed using LightCycler 480 SW 1.5 software. Data were normalized to GAPDH RNA expression and mean values and SDs were determined. Mean values, SD, and *n* values were then used to calculate *P* values in unpaired Student's *t* tests using GraphPad QuickCalcs (GraphPad Software). Graphs were prepared using GraphPad Prism software.

BioStation imaging and data analysis

After wounding, cells were transferred to a Nikon BioStation IMQ equipped with a 20× objective (NA 0.8) and a high-sensitivity 1.3-megapixel cooled monochrome camera for brightfield imaging. Data acquisition typically started 30 min to 1 h after placing the specimens into the BioStation, dependent on how fast the system stabilized at 37°C and 5% CO_2. Data were acquired with BioStation IM software and processed using Nikon Elements software. Manual single cell tracking throughout time frames to determine distance and path length traveled by individual cells in a monolayer at the wound edges was carried out with Nikon Elements AR3.2. To determine average speed, we first averaged individually imaged areas. Individual area data were subsequently averaged as presented in Figure 2, B and C. For area coverage analysis, BioStation nex files were converted to Nikon nd2 files and batch analysis was run using Nikon Elements 4.5. "Field Measurement" measured the biggest inverted area (i.e., the cell-free area) throughout the time frames (settings: 1. Cell: low pass filter, auto contrast, edge detection; 2. Only_biggist_invert_cell: invert, fill holes, filter on object area). Frames were checked manually and were discarded if they could not be analyzed with this method. Area closure was determined as the percentage of the total area of the frame that became covered by migrating cells divided by the length of imaging (typically 1.5 to 3 h). To determine statistical significance, mean values and SDs were determined from the combined data points of at least three independent experiments. Mean values, SD, and *n* values were then used to calculate *P* values in unpaired Student's *t* tests using GraphPad QuickCalcs (GraphPad Software). Graphs were prepared using GraphPad Prism software. The percentage of changes were calculated by setting the control cell data at 100%.

Immunofluorescence staining and fluorescent imaging

Staining was performed essentially as previously described (Cook *et al.*, 2011; Pigati *et al.*, 2013). Briefly, after washing 3× with PBS^{2+} (phosphate-buffered saline [2.67 mM KCl, 1.47 mM KH_2PO_4] plus 0.901 mM Ca^{2+} and 0.493 mM Mg^{2+}), cells were fixed with 3% PFA for 15 min (4% PFA for 20 min for fixed TIRF) at room temperature (RT), followed by a 5-min incubation in PBS^{2+} at RT. If dealing with filter supports, filters were cut out from their holders during this 5-min incubation. Specimens were then blocked for 1 h at RT in 10% goat serum (10% FBS if a goat primary antibody was used), 2% BSA, and 0.4% saponin (0.2% saponin for cells seeded on filter supports) in PBS^{2+}. Primary antibodies were diluted in block solution without serum. Specimens were incubated with primary antibodies for 1 h at RT (or overnight at 4°C for TIRF) followed by five washes over 30 min in block solution without serum. Specimens were then incubated with secondary antibodies and phalloidin—if indicated—diluted in block solution without serum for 1 h at RT, followed by five washes over 30 min in block solution without serum (or just PBS for fixed TIRF). If needed, DAPI was added to the last wash. Specimens were dipped in H_2O and mounted in ProLong Gold (Invitrogen). Specimens for fixed TIRF were kept in PBS at 4°C and imaged the same day. Specimens prepared for STORM were kept in PBS^{2+} at 4°C overnight and imaged the next day.

To obtain 3D galleries, specimens were imaged at RT using Nikon A1 or A1R laser-scanning microscopes equipped with plan Apo λ 100× Oil objectives (NA 1.45) and Nikon A1plus cameras. TIRF was imaged at RT using a Nikon W1 dual cam spinning disk confocal equipped with an Apo TIRF 100× Oil DIC N2 objective (NA 1.49) and a 95B prime Photometrics camera, as well as a Nikon Perfect Focus Ti2 microscope. STORM was imaged at RT using a Nikon X1 spinning disk confocal equipped with an Apo TIRF 100× Oil DIC N2 objective (NA 1.49) and an Andor DU-897 X-6974 camera in STORM buffer (50 mM Tris-HCl, pH 8.0, 10 mM NaCl, 0.5 mg/ml glucose oxidase, 40 µg/ml catalase, 10% glucose, 10 mM mercaptoethylamine). Data were analyzed using Nikon Elements software.

To determine peak intensities for confocal images acquired with A1R microscopes, radial line scans were drawn through representative areas in focused gallery projections. In addition, the average percentage of cell protrusions in which YFP and β1 integrin signals copeaked was determined. Mean values, SDs, and *n* values were used to calculate *P* values in unpaired Student's *t* tests using GraphPad QuickCalcs (GraphPad Software). The percentage of values and peak intensities were plotted with GraphPad Prism software.

STORM analysis included identifying real events using software algorithms to identify blinks of medium brightness and eliminating the first 10 to 20 s of massive photobleaching from the analysis. Identified events were clustered typically at a density of 5 counts in a 70-nm radius. Data were processed and combined for presentation using Adobe Photoshop and Adobe Illustrator. The percentage of cells that expressed HA-tagged AP-1 complexes and gave anti-HA STORM signals was calculated per experiment and averaged. Mean values, SDs, and *n* values (= number of STORM experiments) were used to calculate *P* values in unpaired Student's *t* tests using GraphPad QuickCalcs (GraphPad Software). Graphs were prepared using GraphPad Prism software.

Fixed TIRF data were quantified using the general analysis tool within Nikon Elements 5.2 software for object-based colocalization. To this end, smooth denoising of data and a rolling ball subtraction (1 µm diameter) was chosen, and thresholds were set for the channels to be analyzed to reduce nonspecific background. Threshold settings were kept constant within data sets. Objects within a chosen channel were subsequently automatically identified with the program. We typically set the channel that detected µ1A or µ1B as the reference channel. For example, if µ1B-YFP was stained with 488-labeled secondary antibodies, this would be our reference channel. The program then measured objects in the other channel(s) that overlapped partially or completely with the 488-positive areas. For the analysis, well-formed protrusions of cells at the wound edge were cropped out as areas to be analyzed. On occasion, there were areas that contained 10 or more objects. These were ROIs with oversaturated pixels that were discarded from the analysis. Mean values, SD, and *n* values of the analyses were used to calculate *P* values in unpaired Student's *t* tests using GraphPad QuickCalcs (GraphPad Software). Graphs were prepared using GraphPad Prism software.

Electron microscopy: pre-embedding immunolabeling, silver enhancement, and imaging

After three washes of the specimens in PBS^{2+} (PBS plus Ca^{2+} and Mg^{2+}; see section on immunofluorescence staining), specimens were fixed with 8% PFA (EM grade) in 0.25 M HEPES buffer (pH about 7.1) for 1 h at RT. New fixative was then added followed by an overnight incubation at 4°C. The next day, specimens were washed 3 × for 5 min each in PBS at RT with gentle shaking on a rocker. Specimens were then quenched for 15 min in 50 mM NH_4Cl in PBS, followed by 3 washes in PBS, 5 min each, at RT with gentle shaking. Specimens were blocked with 2% goat serum, 0.1% BSA-c (from Aurion), and 0.2% saponin in PBS for 1 h at RT. Anti-HA antibodies were diluted (1:75) in block solution and incubated with specimens for 1 h at RT followed by 4.5-h at 4°C. Subsequently, specimens were washed 3 × in PBS, 5 min each, at RT with gentle shaking. 1.4-nm gold-labeled secondary goat anti-mouse antibodies were diluted (1:50) in block solution and incubated with the specimens overnight at 4°C. The next day, specimens were washed 3 × in PBS,

5 min each, at RT with gentle shaking. After the last wash, specimens were incubated with 2% glutaraldehyde in PBS for 30 min at RT, followed by 3 washes in PBS, 5 min each, at RT with gentle shaking. Specimens were quenched for 5 min in 50 mM NH_4Cl in deionized water at RT, followed by 2 washes in deionized water, 5 min each, at RT.

The subsequent silver enhancement reaction was carried out in a darkroom. The developer was prepared according to the manufacturer's instruction and 50-µl drops were added to the probes. Reactions were stopped after 10, 12.5 or 15 min by washing 6 × with deionized water, 2 min each, at RT. Samples were immediately postfixed in 1% osmium tetroxide and 3% uranyl acetate, dehydrated in a series of ethanol washes and embedded in Epon 812 resin. The resin blocks were cured for 1 d at 56°C, and glass coverslips were removed from the blocks in liquid nitrogen. Ultrathin 70-nm sections were cut using a Leica UC7 Ultratome, deposited on copper grids and contrasted with Reynolds lead citrate and uranyl acetate. EM data were gathered with a Hitachi HD-2300A Dual EDS Cryo STEM operated at 200 kV utilizing the phase contrast bright field (TE) detector or the high angle annular dark field (HAADF) detector. Images were collected on Gatan Digital Micrograph with a Digiscan system. Images were processed and combined using Adobe Photoshop and Adobe Illustrator.

Statistical analysis was done with ImageJ software. To this end, labels in whole cell images were marked and counted. Next, cells were outlined, and the outside of the cells were cleared before converting the images into binary distance maps with units ranging from 0–255 where '0' marked the surrounding (lateral) plasma membrane and '255' marked the middle of the cells. Distances for individual spots were measured in the ROI manager. Subsequently, the amount of label within the 50, 100, 250 and 500 nm range away from the surrounding plasma membrane was determined using the known scale of images. Data are expressed as percentage of label in 50 or 100 nm with respect to the total counts or within a range of 250 or 500 nm. Mean values, SD, and *n* values were then used to calculate P values in unpaired Student's *t* tests using GraphPad QuickCalcs (GraphPad Software). Graphs were prepared using GraphPad Prism software.

Western blot analysis and coimmunoprecipitations

For Western blot analysis of total cell lysates, cells were seeded at a 1:1 dilution into 6-well plates and grown for 1 d. Cells were washed 2× with ice-cold PBS^{2+} (PBS plus Ca^{2+} and Mg^{2+}; see section on immunofluorescence staining) and 600 µl RIPA buffer (50 mM Tris-HCl, pH 7.6, 150 mM NaCl, 1% Triton X-100, 0.5% deoxycholate, 0.1% SDS, and 1× protease inhibitors [Roche]) was added per well. Subsequently, cells were scraped and passaged 3× through a 22½ G needle and 1-ml syringe, followed by a 30-min incubation on ice. Samples were then spun at 16,100 × *g* for 15 min at 4°C (microcentrifuge, Eppendorf). Supernatants were transferred to new tubes, and protein concentrations were determined using the BCA protein assay (Thermo Fisher Scientific). Protein lysates were analyzed by SDS–PAGE and Western blot using fluorescently labeled secondary antibodies. Specimens were imaged using a Li-Cor Odyssey Blot imager. Representative exposures were assembled and combined using Adobe Photoshop and Adobe Illustrator.

For coimmunoprecipitations, cells were seeded (1:1) into 10-cm plates 1 d prior to the experiment. Cells were washed 2× with PBS^{2+} and 4 ml lysis buffer (50 mM Tris-HCl, pH 7.4, 300 mM NaCl, 1% Triton X-100, 0.1% BSA, 1× protease inhibitors [Roche]) was added to the washed samples. Cells were scraped with a cell scraper and passed 3× through a 22½ G needle and 5-ml syringe. Lysates were incubated on ice for 30 min and spun at 16,100 × *g* for 15 min at 4°C (microcentrifuge, Eppendorf). Lysis supernatants were then incubated for 1 h at 4°C, rotating end-over-end, with relevant antibodies that were prebound to protein G-Sepharose beads. Coimmunoprecipitates were washed 2× with lysis buffer and 1× with lysis buffer without Triton X-100. Samples were analyzed by SDS–PAGE and Western blot using HRP-labeled secondary antibodies and Super-Signal West Pico chemiluminescent substrate (Thermo Fisher Scientific). Films with representative exposure times were scanned. Data were then assembled and combined using Adobe Photoshop and Adobe Illustrator.

For immunoisolations of clathrin-coated vesicles, cells were split (1:1) into six 20-cm dishes. Typically 2 d after seeding, cells were wounded by scratching the monolayers multiple times with a P1000 pipette tip and incubated for 1.5 h. Cells were then washed twice with PBS^{2+}, and 2 ml buffer D (10 mM HEPES, 150 mM NaCl, 0.5 mM $MgCl_2$, 1× protease inhibitors [mini tablets from Pierce], and 0.02 [wt/vol] NaN_3) was added. Cells were scrapped off the plate, combined, and homogenized with a cell cracker followed by a clarifying spin in an Allegra D centrifuge (Beckman) at 4°C for 30 min at 5000 × *g*. Supernatants were harvested and adjusted with Triton X-100 to a final concentration of 1% and spun for 1 h in a MAX-E tabletop ultracentrifuge (Beckman) at 4°C and 100,000 × *g* (47,000 rpm, MLA80 rotor). Pellets were resuspended in 3 ml buffer D^+ (buffer D plus 250 mM sucrose) and subjected to immunoprecipitations with goat anti-GFP antibodies (generic goat IgGs as control) or mouse anti-γ-adaptin antibodies (mouse hybridoma C7 antibodies as control) bound to protein G-Sepharose beads (Fisher Scientific). Samples were rotated end-over-end at 4°C for 2 h and washed 2× in buffer D^+ and 1× in PBS. Immunoprecipitates were denatured in SDS sample buffer, vigorously shaken for 5 min at RT, boiled, and analyzed by SDS–PAGE and Western blot using fluorescently labeled secondary antibodies followed by analysis using a Li-Cor Odyssey Blot imager. Representative exposures were assembled and combined using Adobe Photoshop and Adobe Illustrator.

ACKNOWLEDGMENTS

We thank Linton Traub for anti-µ1 antibodies, Samuel Romo for technical assistance, and our Northwestern colleagues Constadina Arvanitis, David Kirchenbuechler, Farida Korobova, Wensheng Liu, Joshua Rappoport (now at Boston College), Eric Roth, and Lili Zheng for advice and discussions. This work was supported by an A*STAR Singapore postdoctoral fellowship to S.F.A., by the National Institutes of Health grant GM070736 to H.F., and cores of the Skin Biology and Diseases Resource-based Center (grant P30AR075049) and Center for Advanced Microscopy (grants NCI CCSG P30 CA060553 awarded to the Robert H Lurie Comprehensive Cancer Center and NCRR 1S10 RR031680). Further, this work made use of the BioCryo facility of Northwestern University's NUANCE Center, which has received support from the Soft and Hybrid Nanotechnology Experimental (SHyNE) Resource (National Science Foundation [NSF] ECCS-1542205); the MRSEC program (NSF DMR-1720139) at the Materials Research Center; the International Institute for Nanotechnology (IIN); and the State of Illinois, through the IIN. It also made use of the CryoCluster equipment, which has received support from the MRI program (NSF DMR-1229693).

REFERENCES

Altschuler Y, Liu S, Katz L, Tang K, Hardy S, Brodsky F, Apodaca G, Mostov K (1999). ADP-ribosylation factor 6 and endocytosis at the apical surface of Madin-Darby canine kidney cells. J Cell Biol 147, 7–12.

Anderson E, Maday S, Sfakianos J, Hull M, Winckler B, Sheff D, Fölsch H, Mellman I (2005). Transcytosis of NgCAM in epithelial cells reflects

differential signal recognition on the endocytic and secretory pathways. J Cell Biol 170, 595–605.
Ang AL, Taguchi T, Francis S, Fölsch H, Murrells LJ, Pypaert M, Warren G, Mellman I (2004). Recycling endosomes can serve as intermediates during transport from the Golgi to the plasma membrane of MDCK cells. J Cell Biol 167, 531–543.
Ang SF, Fölsch H (2012). The role of secretory and endocytic pathways in the maintenance of cell polarity. Essays Biochem 53, 29–39.
Boehm M, Bonifacino JS (2001). Adaptins: the final recount. Mol Biol Cell 12, 2907–2920.
Boulant S, Kural C, Zeeh JC, Ubelmann F, Kirchhausen T (2011). Actin dynamics counteract membrane tension during clathrin-mediated endocytosis. Nat Cell Biol 13, 1124–1131.
Brockbank EC, Bridges J, Marshall CJ, Sahai E (2005). Integrin beta1 is required for the invasive behaviour but not proliferation of squamous cell carcinoma cells in vivo. Br J Cancer 92, 102–112.
Caceres PS, Gravotta D, Zager PJ, Dephoure N, Rodriguez-Boulan E (2019). Quantitative proteomics of MDCK cells identify unrecognized roles of clathrin adaptor AP-1 in polarized distribution of surface proteins. Proc Natl Acad Sci USA 116, 11796–11805.
Cancino J, Torrealba C, Soza A, Yuseff MI, Gravotta D, Henklein P, Rodriguez-Boulan E, Gonzalez A (2007). Antibody to AP1B adaptor blocks biosynthetic and recycling routes of basolateral proteins at recycling endosomes. Mol Biol Cell 18, 4872–4884.
Collins BM, McCoy AJ, Kent HM, Evans PR, Owen DJ (2002). Molecular architecture and functional model of the endocytic AP2 complex. Cell 109, 523–535.
Cook RN, Ang SF, Kang RS, Fölsch H (2011). Analyzing the function of small GTPases by microinjection of plasmids into polarized epithelial cells. J Vis Exp.
Daro E, van der Sluijs P, Galli T, Mellman I (1996). Rab4 and cellubrevin define different early endosome populations on the pathway of transferrin receptor recycling. Proc Natl Acad Sci USA 93, 9559–9564.
De Franceschi N, Arjonen A, Elkhatib N, Denessiouk K, Wrobel AG, Wilson TA, Pouwels J, Montagnac G, Owen DJ, Ivaska J (2016). Selective integrin endocytosis is driven by interactions between the integrin alpha-chain and AP2. Nat Struct Mol Biol 23, 172–179.
Deborde S, Perret E, Gravotta D, Deora A, Salvarezza S, Schreiner R, Rodriguez-Boulan E (2008). Clathrin is a key regulator of basolateral polarity. Nature 452, 719–723.
DiNitto JP, Delprato A, Gabe Lee MT, Cronin TC, Huang S, Guilherme A, Czech MP, Lambright DG (2007). Structural basis and mechanism of autoregulation in 3-phosphoinositide-dependent Grp1 family Arf GTPase exchange factors. Mol Cell 28, 569–583.
Di Paolo G, De Camilli P (2006). Phosphoinositides in cell regulation and membrane dynamics. Nature 443, 651–657.
Doray B, Lee I, Knisely J, Bu G, Kornfeld S (2007). The gamma/sigma1 and alpha/sigma2 hemicomplexes of clathrin adaptors AP-1 and AP-2 harbor the dileucine recognition site. Mol Biol Cell 18, 1887–1896.
Dunn KW, Kamocka MM, McDonald JH (2011). A practical guide to evaluating colocalization in biological microscopy. Am J Physiol 300, C723–C742.
Elkhatib N, Bresteau E, Baschieri F, Rioja AL, van Niel G, Vassilopoulos S, Montagnac G (2017). Tubular clathrin/AP-2 lattices pinch collagen fibers to support 3D cell migration. Science 356.
Ezratty EJ, Bertaux C, Marcantonio EE, Gundersen GG (2009). Clathrin mediates integrin endocytosis for focal adhesion disassembly in migrating cells. J Cell Biol 187, 733–747.
Fields IC, King SM, Shteyn E, Kang RS, Fölsch H (2010). Phosphatidylinositol 3,4,5-trisphosphate localization in recycling endosomes is necessary for AP-1B-dependent sorting in polarized epithelial cells. Mol Biol Cell 21, 95–105.
Fields IC, Shteyn E, Pypaert M, Proux-Gillardeaux V, Kang RS, Galli T, Fölsch H (2007). v-SNARE cellubrevin is required for basolateral sorting of AP-1B-dependent cargo in polarized epithelial cells. J Cell Biol 177, 477–488.
Fletcher SJ, Poulter NS, Haining EJ, Rappoport JZ (2012). Clathrin-mediated endocytosis regulates occludin, and not focal adhesion, distribution during epithelial wound healing. Biol Cell 104, 238–256.
Fölsch H (2015a). Analyzing the role of AP-1B in polarized sorting from recycling endosomes in epithelial cells. Method Cell Biol 130, 289–305.
Fölsch H (2015b). Role of the epithelial cell-specific clathrin adaptor complex AP-1B in cell polarity. Cell Logist 5, e1074331.
Fölsch H, Mattila PE, Weisz OA (2009). Taking the scenic route: biosynthetic traffic to the plasma membrane in polarized epithelial cells. Traffic 10, 972–981.
Fölsch H, Ohno H, Bonifacino JS, Mellman I (1999). A novel clathrin adaptor complex mediates basolateral targeting in polarized epithelial cells. Cell 99, 189–198.
Fölsch H, Pypaert M, Maday S, Pelletier L, Mellman I (2003). The AP-1A and AP-1B clathrin adaptor complexes define biochemically and functionally distinct membrane domains. J Cell Biol 163, 351–362.
Fölsch H, Pypaert M, Schu P, Mellman I (2001). Distribution and Function of AP-1 Clathrin Adaptor Complexes in Polarized Epithelial Cells. J Cell Biol 152, 595–606.
Franca-Koh J, Kamimura Y, Devreotes PN (2007). Leading-edge research: PtdIns(3,4,5)P3 and directed migration. Nat Cell Biol 9, 15–17.
Galli T, Chilcote T, Mundigl O, Binz T, Niemann H, De Camilli P (1994). Tetanus toxin-mediated cleavage of cellubrevin impairs exocytosis of transferrin receptor-containing vesicles in CHO cells. J Cell Biol 125, 1015–1024.
Gan Y, McGraw TE, Rodriguez-Boulan E (2002). The epithelial-specific adaptor AP1B mediates post-endocytic recycling to the basolateral membrane. Nat Cell Biol 4, 605–609.
Gassama-Diagne A, Yu W, ter Beest M, Martin-Belmonte F, Kierbel A, Engel J, Mostov K (2006). Phosphatidylinositol-3,4,5-trisphosphate regulates the formation of the basolateral plasma membrane in epithelial cells. Nat Cell Biol 8, 963–970.
Gautier JJ, Lomakina ME, Bouslama-Oueghlani L, Derivery E, Beilinson H, Faigle W, Loew D, Louvard D, Echard A, Alexandrova AY, *et al.* (2011). Clathrin is required for Scar/Wave-mediated lamellipodium formation. J Cell Sci 124, 3414–3427.
Gravotta D, Carvajal-Gonzalez JM, Mattera R, Deborde S, Banfelder JR, Bonifacino JS, Rodriguez-Boulan E (2012). The clathrin adaptor AP-1A mediates basolateral polarity. Dev Cell 22, 811–823.
Gravotta D, Deora A, Perret E, Oyanadel C, Soza A, Schreiner R, Gonzalez A, Rodriguez-Boulan E (2007). AP1B sorts basolateral proteins in recycling and biosynthetic routes of MDCK cells. Proc Natl Acad Sci USA 104, 1564–1569.
Gu FL, Cai SL, Cai BJ, Wu CP (1991). Cellular origin of renal cell carcinoma—an immunohistological study on monoclonal antibodies. Scand J Urol Nephrol Suppl 138, 203–206.
Guo X, Mattera R, Ren X, Chen Y, Retamal C, Gonzalez A, Bonifacino JS (2013). The adaptor protein-1 mu1B subunit expands the repertoire of basolateral sorting signal recognition in epithelial cells. Dev Cell 27, 353–366.
Hase K, Nakatsu F, Ohmae M, Sugihara K, Shioda N, Takahashi D, Obata Y, Furusawa Y, Fujimura Y, Yamashita T, *et al.* (2013). AP-1B-mediated protein sorting regulates polarity and proliferation of intestinal epithelial cells in mice. Gastroenterology 145, 625–635.
He G, Gupta S, Yi M, Michaely P, Hobbs HH, Cohen JC (2002). ARH is a modular adaptor protein that interacts with the LDL receptor, clathrin, and AP-2. J Biol Chem 277, 44044–44049.
Hirst J, Robinson MS (1998). Clathrin and adaptors. Biochim Biophys Acta 1404, 173–193.
Holthofer H, Miettinen A, Paasivuo R, Lehto VP, Linder E, Alfthan O, Virtanen I (1983). Cellular origin and differentiation of renal carcinomas. A fluorescence microscopic study with kidney-specific antibodies, antiintermediate filament antibodies, and lectins. Lab Invest 49, 317–326.
Hönig E, Ringer K, Dewes J, von Mach T, Kamm N, Kreitzer G, Jacob R (2018). Galectin-3 modulates the polarized surface delivery of beta1-integrin in epithelial cells. J Cell Sci 131.
Horton ER, Humphries JD, James J, Jones MC, Askari JA, Humphries MJ (2016). The integrin adhesome network at a glance. J Cell Sci 129, 4159–4163.
Hwang S, Zimmerman NP, Agle KA, Turner JR, Kumar SN, Dwinell MB (2012). E-cadherin is critical for collective sheet migration and is regulated by the chemokine CXCL12 protein during restitution. J Biol Chem 287, 22227–22240.
Janvier K, Kato Y, Boehm M, Rose JR, Martina JA, Kim BY, Venkatesan S, Bonifacino JS (2003). Recognition of dileucine-based sorting signals from HIV-1 Nef and LIMP-II by the AP-1 gamma-sigma1 and AP-3 delta-sigma3 hemicomplexes. J Cell Biol 163, 1281–1290.
Kang RS, Fölsch H (2011). ARH cooperates with AP-1B in the exocytosis of LDLR in polarized epithelial cells. J Cell Biol 193, 51–60.
Kural C, Tacheva-Grigorova SK, Boulant S, Cocucci E, Baust T, Duarte D, Kirchhausen T (2012). Dynamics of intracellular clathrin/AP1- and clathrin/AP3-containing carriers. Cell Rep 2, 1111–1119.
Larjava H, Peltonen J, Akiyama SK, Yamada SS, Gralnick HR, Uitto J, Yamada KM (1990). Novel function for beta 1 integrins in keratinocyte cell-cell interactions. J Cell Biol 110, 803–815.

Ling K, Bairstow SF, Carbonara C, Turbin DA, Huntsman DG, Anderson RA (2007). Type Igamma phosphatidylinositol phosphate kinase modulates adherens junction and E-cadherin trafficking via a direct interaction with mu1B adaptin. J Cell Biol 176, 343–353.
Martensson S, Brunmark C, Ohlsson L, Bak-Jensen E, Butkowski R, Boketoft A, Wieslander J (1995). Heterogeneity of renal carcinoma. Nephrol Dial Transplant 10, 1637–1643.
Mattheyses AL, Simon SM, Rappoport JZ (2010). Imaging with total internal reflection fluorescence microscopy for the cell biologist. J Cell Sci 123, 3621–3628.
Mellman I, Nelson WJ (2008). Coordinated protein sorting, targeting and distribution in polarized cells. Nat Rev 9, 833–845.
Mimura M, Masuda A, Nishiumi S, Kawakami K, Fujishima Y, Yoshie T, Mizuno S, Miki I, Ohno H, Hase K, *et al*. (2011). AP1B plays an important role in intestinal tumorigenesis with the truncating mutation of an APC gene. Int J Cancer 130, 1011–1020.
Miranda KC, Khromykh T, Christy P, Le TL, Gottardi CJ, Yap AS, Stow JL, Teasdale RD (2001). A dileucine motif targets E-cadherin to the basolateral cell surface in Madin-Darby canine kidney and LLC-PK1 epithelial cells. J Biol Chem 276, 22565–22572.
Mishra SK, Watkins SC, Traub LM (2002). The autosomal recessive hypercholesterolemia (ARH) protein interfaces directly with the clathrin-coat machinery. Proc Natl Acad Sci USA 99, 16099–16104.
Moreno-Layseca P, Icha J, Hamidi H, Ivaska J (2019). Integrin trafficking in cells and tissues. Nat Cell Biol 21, 122–132.
Moser M, Legate KR, Zent R, Fassler R (2009). The tail of integrins, talin, and kindlins. Science 324, 895–899.
Nakatsu F, Ohno H (2003). Adaptor protein complexes as the key regulators of protein sorting in the post-Golgi network. Cell Struct Funct 28, 419–429.
Nokes RL, Fields IC, Collins RN, Fölsch H (2008). Rab13 regulates membrane trafficking between TGN and recycling endosomes in polarized epithelial cells. J Cell Biol 182, 845–853.
Ohno H, Tomemori T, Nakatsu F, Okazaki Y, Aguilar RC, Fölsch H, Mellman I, Saito T, Shirasawa T, Bonifacino JS (1999). Mu1B, a novel adaptor medium chain expressed in polarized epithelial cells. FEBS Lett 449, 215–220.
Owen DJ, Evans PR (1998). A structural explanation for the recognition of tyrosine-based endocytotic signals. Science 282, 1327–1332.
Paul NR, Jacquemet G, Caswell PT (2015). Endocytic trafficking of integrins in cell migration. Curr Biol 25, R1092–R1105.
Pearse BM (1982). Coated vesicles from human placenta carry ferritin, transferrin, and immunoglobulin G. Proc Natl Acad Sci USA 79, 451–455.
Pearse BM, Robinson MS (1984). Purification and properties of 100-kd proteins from coated vesicles and their reconstitution with clathrin. EMBO J 3, 1951–1957.
Pigati L, Kang RS, Fölsch H (2013). Using replication defective viruses to analyze membrane trafficking in polarized epithelial cells. Methods Cell Biol 118, 125–137.
Proux-Gillardeaux V, Gavard J, Irinopoulou T, Mege RM, Galli T (2005). Tetanus neurotoxin-mediated cleavage of cellubrevin impairs epithelial cell migration and integrin-dependent cell adhesion. Proc Natl Acad Sci USA 102, 6362–6367.
Ratcliffe CD, Sahgal P, Parachoniak CA, Ivaska J, Park M (2016). Regulation of cell migration and beta1 integrin trafficking by the endosomal adaptor GGA3. Traffic 17, 670–688.
Rodriguez-Boulan E, Müsch A, Le Bivic A (2004). Epithelial trafficking: new routes to familiar places. Curr Opin Cell Biol 16, 436–442.
Roush DL, Gottardi CJ, Naim HY, Roth MG, Caplan MJ (1998). Tyrosine-based membrane protein sorting signals are differentially interpreted by polarized Madin-Darby canine kidney and LLC-PK1 epithelial cells. J Biol Chem 273, 26862–26869.
Sahgal P, Alanko J, Icha J, Paatero I, Hamidi H, Arjonen A, Pietila M, Rokka A, Ivaska J (2019). GGA2 and RAB13 promote activity-dependent beta1-integrin recycling. J Cell Sci 132.
Santy LC, Casanova JE (2001). Activation of ARF6 by ARNO stimulates epithelial cell migration through downstream activation of both Rac1 and phospholipase D. J Cell Biol 154, 599–610.
Schmoranzer J, Kreitzer G, Simon SM (2003). Migrating fibroblasts perform polarized, microtubule-dependent exocytosis towards the leading edge. J Cell Sci 116, 4513–4519.
Schreiner R, Frindt G, Diaz F, Carvajal-Gonzalez JM, Perez Bay AE, Palmer LG, Marshansky V, Brown D, Philp NJ, Rodriguez-Boulan E (2010). The absence of a clathrin adapter confers unique polarity essential to proximal tubule function. Kidney Int 78, 382–388.
Shteyn E, Pigati L, Fölsch H (2011). Arf6 regulates AP-1B-dependent sorting in polarized epithelial cells. J Cell Biol 194, 873–887.
Toomre D, Steyer JA, Keller P, Almers W, Simons K (2000). Fusion of constitutive membrane traffic with the cell surface observed by evanescent wave microscopy. J Cell Biol 149, 33–40.
Traub LM (2003). Sorting it out: AP-2 and alternate clathrin adaptors in endocytic cargo selection. J Cell Biol 163, 203–208.
Traub LM (2009). Tickets to ride: selecting cargo for clathrin-regulated internalization. Nat Rev 10, 583–596.
van de Linde S, Loschberger A, Klein T, Heidbreder M, Wolter S, Heilemann M, Sauer M (2011). Direct stochastic optical reconstruction microscopy with standard fluorescent probes. Nat Protoc 6, 991–1009.
Wang X, Chen Z, Mettlen M, Noh J, Schmid SL, Danuser G (2020). DASC, a sensitive classifier for measuring discrete early stages in clathrin-mediated endocytosis. eLife 9.
Wang YJ, Wang J, Sun HQ, Martinez M, Sun YX, Macia E, Kirchhausen T, Albanesi JP, Roth MG, Yin HL (2003). Phosphatidylinositol 4 phosphate regulates targeting of clathrin adaptor AP-1 complexes to the Golgi. Cell 114, 299–310.
Weisz OA, Fölsch H (2016). Molecular mechanisms of apical and basolateral sorting in polarized epithelial cells. In: Ion Channels and Transporters of Epithelia in Health and Disease, New York: Springer-Verlag, 279–302.
Weisz OA, Rodriguez-Boulan E (2009). Apical trafficking in epithelial cells: signals, clusters and motors. J Cell Sci 122, 4253–4266.
Winograd-Katz SE, Fassler R, Geiger B, Legate KR (2014). The integrin adhesome: from genes and proteins to human disease. Nat Rev 15, 273–288.
Zhao Y, Keen JH (2008). Gyrating clathrin: highly dynamic clathrin structures involved in rapid receptor recycling. Traffic 9, 2253–2264.